



HAL
open science

A micromechanically consistent energy estimate for polycrystalline shape-memory alloys, II: Application to Lüders-type strain localization

Michaël Peigney

► **To cite this version:**

Michaël Peigney. A micromechanically consistent energy estimate for polycrystalline shape-memory alloys, II: Application to Lüders-type strain localization. *Journal of the Mechanics and Physics of Solids*, 2023, 173, pp.105220. 10.1016/j.jmps.2023.105220 . hal-04223062v2

HAL Id: hal-04223062

<https://enpc.hal.science/hal-04223062v2>

Submitted on 5 Mar 2024

HAL is a multi-disciplinary open access archive for the deposit and dissemination of scientific research documents, whether they are published or not. The documents may come from teaching and research institutions in France or abroad, or from public or private research centers.

L'archive ouverte pluridisciplinaire **HAL**, est destinée au dépôt et à la diffusion de documents scientifiques de niveau recherche, publiés ou non, émanant des établissements d'enseignement et de recherche français ou étrangers, des laboratoires publics ou privés.

A micromechanically consistent energy estimate for polycrystalline shape-memory alloys. II - Application to Lüders-type strain localization.

Michaël Peigney

Lab Navier, Univ Gustave Eiffel, ENPC, CNRS, F-77447 Marne la Vallée, France

Abstract

We make use of a micromechanical energy estimate proposed in the companion paper (Peigney, 2023) to study strain Lüders-like localization in polycrystalline NiTi specimen under tension. Under the assumption that only the most favorably oriented martensitic variant is active in each grain, it is shown that the homogeneous equilibrium problem can be solved analytically for fiber textures (as commonly found in drawn wires or tubes) and more generally for transversely isotropic textures. This leads to an analytical condition for strain localization that admits an explicit expression in terms of the elastic moduli, the lattice parameters and simple statistical information on the texture. The obtained condition allows one to understand what is distinctive about NiTi compared to other shape memory alloys and why strain localization does not appear in compression. In the cases when strain localization is predicted, several quantities of interest such as the strain gap between initiation of phase transformation and localization, the stress drop at the onset of localization and the inclination of the bands can be derived. The results obtained from the presented analytical solution are compared with numerical simulations performed by taking several active variants in each grain into account and considering imperfect transversely isotropic textures. It is found that the presented analytical solution gives a fairly accurate estimate of the response of 100 (and more)-grain aggregates. Taking several active variants per crystalline orientation does not impact the localization condition significantly but gives values of the strain gaps between initiation and localization that are closer to the experimental values reported in the literature.

Keywords: Shape memory alloys, Strain localization, Lüders band, Micromechanics

Email address: michael.peigney@polytechnique.org (Michaël Peigney)

1. Introduction

NiTi belongs to the class of Shape Memory Alloys (SMAs), whose distinctive properties stem from the diffusionless stress-induced or temperature-induced phase transformation between austenite and martensite. Polycrystalline NiTi specimen under tension tend to deform via the nucleation and propagation of fronts separating highly strained regions from lowly strained regions. This phenomenon is well documented and shows some similarity with Lüders bands in mild steels (Piobert, 1842; Lüders, 1860; Butler, 1962; Kyriakides and Miller, 2000). In wires or bars, the highly strained regions take the form of propagating hourglass-shaped necks (Churchill et al., 2009). Band fronts in flat-shape specimen are inclined at approximately 55° to the load axis (Shaw and Kyriakides, 1997; Daly et al., 2007) whereas in tubes they are spiral-shaped with an inclination in the range $55 - 61^\circ$ (Sun and Li, 2002; Reedlunn et al., 2014). Experiments carefully designed to minimize grip effects show a significant stress drop (close to 100 MPa) at the onset of strain localization (Churchill et al., 2009).

Deformation in monocrystalline SMAs is also localized and in that case the situation is rather well understood: band fronts separate austenitic regions from martensitic regions and the inclination of those austenite-martensite interfaces can be predicted by the Crystallography Theory of Martensite (CTM) (Shield, 1995). The nucleation of fronts in monocrystalline SMAs coincides with the initiation of phase transformation. The mechanism of localization in polycrystalline NiTi is more complex and not so well understood. Strain field measurement suggest that austenite and martensite are both present in the highly strained regions as well as in the lowly strain edregions (Daly et al., 2007). The inclination of the fronts cannot be explained by CTM (Liu et al., 1999), which confirms that band fronts in polycrystalline SMAs are not austenite-martensite interfaces. Several experiments suggest that phase transformation actually starts before localization occurs (Daly et al., 2007; Brinson et al., 2004). Lüders-type deformation has been observed only in polycrystalline NiTi and not in other common polycrystalline SMAs such as CuZnAl or CuAlNi. Moreover, Lüders-type deformation is not observed in compression of polycrystalline NiTis (or other polycrystalline SMAs): in that case, the deformation remains homogeneous throughout the specimen.

Modelling Lüders-like deformation in SMAs is most commonly achieved by introducing some softening (or any other destabilizing effect) in the constitutive equations, see e.g. Shaw (2000); Iadicola and Shaw (2004); Alessi and Pham (2016) for some examples. This is usually done in an *ad hoc* fashion and the softening parameters

need to be fitted from experiments on a case-by-case basis. Such an *ad hoc* approach has the downside of not explaining why Lüders-like deformation only appear in polycrystalline NiTi, for instance. There is a missing link between the softening parameters and descriptors of the phase transformation and polycrystalline texture. In principle, adopting a micromechanical approach should allow one to recover that missing link. The guiding idea is to start from the constitutive equations of each individual phase at the microscopic level and to obtain the macroscopic (or effective) constitutive relation of a polycrystal via some upscaling strategy. Any destabilizing effect at the macroscopic scale should therefore appear "naturally" from microscopic and textural descriptors. Such a micromechanical approach to strain localization in polycrystalline SMAs has been proposed by Sittner et al. (2005). In the work of Sittner et al. (2005), a 1D heuristic model was used for the stress redistribution between grains and strain localization was interpreted as a geometric instability detected via Considère's criterion (Considère, 1885). The approach adopted in this paper is similar in spirit to that of Sittner et al. (2005), except that we make use of a 3D micromechanical model and interpret strain localization as a material instability detected via Hill's criterion (Hill, 1958). The model we use is an estimate of the effective energy proposed in a companion paper (Peigney, 2023). Adopting the framework of elastic energy minimization and assuming a linear elastic behavior at the microscopic scale for each phase, the effective energy is obtained by means of relaxation and homogenization. Except in few special cases, the exact expression of the effective energy remains elusive but rigorous bounds have been proposed (Smyshlyaev and Willis, 1998; Govindjee et al., 2003; Hackl and Heinen, 2008; Peigney, 2008, 2009, 2013a,b). The energy model proposed in Peigney (2023) satisfies known lower and upper bounds and tentatively gives an accurate estimate of the effective energy of polycrystalline SMAs, taking both intra- and inter-grain constraints into account. The model parameters are related only to the microscopic energy in each phase (elastic moduli, lattice parameters, latent heat) and to the texture of the polycrystal (orientation distribution function).

Compared to phenomenological models, 3D micromechanical models for polycrystalline SMAs have a relatively complex mathematical structure and the model used in this paper is no exception. For a polycrystal with a significant number of grains, calculating the material response under tensile loading is challenging. Besides computational issues, such direct numerical calculations are not very enlightening because they do not clearly show what the main material parameters potentially governing strain localization are. Those issues can be overcome by introducing two ideas. The first idea is to make the approximation that a single martensitic variant (namely, the most favorably oriented variant with respect to the loading direction) is active in

each grain. That assumption is actually commonly used in micromechanical models of polycrystalline SMAs wires and bars under tension (Nae et al., 2002; Sittner et al., 2005; Hannequart et al., 2019). The second idea is to take some information on the textures of interest into account by considering transversely isotropic textures. Textures commonly found in drawn wires or tubes are indeed not arbitrary and generally show a strong $\langle 111 \rangle \parallel \mathbf{u}_1$ fiber component where \mathbf{u}_1 is along the axis of the wire (or tube) (Reedlunn et al., 2020). Using those two ideas, it turns out that the minimization problem defining the material response in tension can be solved exactly. That key part of the paper is detailed in Sect. 3. From the obtained solution, one can derive an analytical condition for strain localization to occur (Sect. 4). That condition takes a relatively simple expression, depending on the texture through the average value and standard deviation of the uniaxial transformation strain over the grains. The obtained condition allows one to understand what is distinctive about NiTi and why Lüders-like deformation does not appear in compression. In cases where strain localization is predicted, several meaningful quantities can be derived, such as the strain gap between initiation and localization, the stress drop at localization, the inclination of the bands. Some comparison with numerical simulations are presented in Sect. 5 to investigate how the picture is changed when several variants are active in each grain and the texture is not perfectly transversely isotropic. Sect. 6 closes the paper with concluding remarks.

2. Equilibrium in strain-driven tension

2.1. General considerations

Consider the equilibrium problem of an elastic cylinder under strain-driven tension in isothermal conditions. Let $(\mathbf{u}_1, \mathbf{u}_2, \mathbf{u}_3)$ be an orthonormal basis such that the cylinder occupies the domain $\Omega = [0, L] \times S$ where $S \subset \text{Vect}(\mathbf{u}_2, \mathbf{u}_3)$ is the section. Note that \mathbf{u}_1 is along the axis of the cylinder. Adopting the geometrically linear setting, the free energy density Ψ of the constitutive material is a function of the linearized strain $\boldsymbol{\varepsilon}$. Equilibrium states are defined by the local equations

$$\begin{aligned} \boldsymbol{\sigma} &= \frac{\partial \Psi}{\partial \boldsymbol{\varepsilon}}(\boldsymbol{\varepsilon}), \\ \text{div } \boldsymbol{\sigma} &= 0 \text{ in } \Omega, \\ \boldsymbol{\sigma} \cdot \mathbf{n} &= 0 \text{ on } [0, L] \times \delta S, \\ \boldsymbol{\sigma} \cdot \mathbf{u}_1 &\parallel \mathbf{u}_1 \text{ on } \{0, L\} \times S, \\ \boldsymbol{\varepsilon} &\in \mathcal{K} \end{aligned} \tag{1}$$

where

$$\mathcal{K} = \left\{ \boldsymbol{\varepsilon} = \frac{1}{2}(\nabla \boldsymbol{\xi} + \nabla^T \boldsymbol{\xi}) : \xi_1 = 0 \text{ for } x_1 = 0, \xi_1 = \varepsilon_{11}L \text{ for } x_1 = L \right\} \tag{2}$$

is the space of admissible strain fields and the superscript T denotes the transpose operator. In (2), the loading parameter is the average axial strain ε_{11} . Homogeneous solutions to (1) are obtained by looking for the values $\boldsymbol{\varepsilon}^*$ that satisfy $\varepsilon_{11}^* = \varepsilon_{11}$ and

$$\frac{\partial \Psi}{\partial \boldsymbol{\varepsilon}}(\boldsymbol{\varepsilon}^*) = \sigma_{11} \mathbf{u}_1 \otimes \mathbf{u}_1 \quad (3)$$

for some σ_{11} . The corresponding stress field $\boldsymbol{\sigma} = \sigma_{11} \mathbf{u}_1 \otimes \mathbf{u}_1$ is uniaxial in the direction \mathbf{u}_1 . Eq. (3) is representative of the local state in the gauge length of a material specimen submitted to a standard tension test, prior to any strain localization. For any given ε_{11} , assume that the strain $\boldsymbol{\varepsilon}^*$ solving (3) is unique. The curve $\varepsilon_{11} \mapsto \sigma_{11}$ is the stress-strain curve that would be measured in a strain-driven tension experiment provided the stress and strain fields are indeed uniform in the gauge length of the tested specimen. Depending on the free energy density Ψ and the applied strain ε_{11} , the homogeneous equilibrium state may be unstable and bifurcate to an inhomogeneous solution to (1). Hill's criterion (Hill, 1958; Drucker, 1959) gives a sufficient criterion for stability: if $\partial^2 \Psi / \partial \boldsymbol{\varepsilon}^2$ is positive definite then the homogeneous equilibrium is stable. If that condition is not satisfied, i.e. if

$$\mathbf{d} : \frac{\partial^2 \Psi}{\partial \boldsymbol{\varepsilon}^2}(\boldsymbol{\varepsilon}^*) : \mathbf{d} \leq 0 \quad (4)$$

for some non-zero symmetric second-order tensor \mathbf{d} , then instability may occur. Eq. (4) is satisfied at any point of negative tangent modulus $d\sigma_{11}/d\varepsilon_{11} \leq 0$ on the stress-strain curve $\varepsilon_{11} \mapsto \sigma_{11}$. Differentiating (3) yields indeed

$$\frac{\partial^2 \Psi}{\partial \boldsymbol{\varepsilon}^2}(\boldsymbol{\varepsilon}^*) : \frac{d\boldsymbol{\varepsilon}^*}{d\varepsilon_{11}} = \frac{d\sigma_{11}}{d\varepsilon_{11}} \mathbf{u}_1 \otimes \mathbf{u}_1.$$

Projecting the above equation on $d\boldsymbol{\varepsilon}^*/d\varepsilon_{11}$ and noting that $d\varepsilon_{11}^*/d\varepsilon_{11} = 1$, we obtain

$$\frac{d\boldsymbol{\varepsilon}^*}{d\varepsilon_{11}} : \frac{\partial^2 \Psi}{\partial \boldsymbol{\varepsilon}^2}(\boldsymbol{\varepsilon}^*) : \frac{d\boldsymbol{\varepsilon}^*}{d\varepsilon_{11}} = \frac{d\sigma_{11}}{d\varepsilon_{11}}.$$

If $d\sigma_{11}/d\varepsilon_{11} \leq 0$ then (65) is satisfied by the tensor

$$\mathbf{d} = \frac{d\boldsymbol{\varepsilon}^*}{d\varepsilon_{11}}. \quad (5)$$

At the onset of instability, the tensor \mathbf{d} in (5) provides some information on the bifurcated state. The condition for a shear band to appear is indeed that \mathbf{d} satisfies the Hadamard compatibility conditions, i.e. that $\mathbf{d} = \mathbf{a} \otimes \mathbf{n} + \mathbf{n} \otimes \mathbf{a}$ for some

vectors (\mathbf{a}, \mathbf{n}) . If \mathbf{d} does not satisfy the Hadamard compatibility conditions then a diffuse deformation mode, such as necking, is expected (see e.g. Besson et al. (2009) and references therein for general theoretical results on strain localization). In view of those considerations, a possible plan for investigating strain localization in strain-driven tension is the following:

1. solve (3) as a function of ε_{11} to obtain the stress-strain curve $\varepsilon_{11} \mapsto \sigma_{11}$ corresponding to homogeneous equilibrium.
2. check if $d\sigma_{11}/d\varepsilon_{11} \leq 0$ at some point on the stress-strain curve, in which case the homogeneous equilibrium may be unstable.
3. at the onset of instability, check if the tensor \mathbf{d} in (5) satisfies the Hadamard compatibility conditions, in order to detect whether localized deformation (shear banding) or diffuse deformation (necking) is more likely.

Carrying out that plan requires to specify the constitutive material and the expression of the free energy density Ψ . From now on, we consider a polycrystalline shape memory alloy as the constitutive material and we adopt the expression proposed in Peigney (2023) for the free energy density Ψ .

2.2. Energy model

Table 1: Transformation strains in representative shape-memory alloys

Symmetry of martensite	n	$\boldsymbol{\tau}_1^0$	example	lattice parameters
Monoclinic-I	12	$\begin{pmatrix} \alpha_l & \delta_l & \epsilon_l \\ \delta_l & \alpha_l & \epsilon_l \\ \epsilon_l & \epsilon_l & \beta_l \end{pmatrix}$	NiTi	$\alpha_l = 0.0243, \beta_l = -0.0437,$ $\delta_l = 0.0580, \epsilon_l = 0.0427$
Monoclinic-II	12	$\begin{pmatrix} \alpha_l + \epsilon_l & \delta_l & 0 \\ \delta_l & \alpha_l - \epsilon_l & 0 \\ 0 & 0 & \beta_l \end{pmatrix}$	CuZnAl	$\alpha_l = 0.0483, \beta_l = -0.0907,$ $\delta_l = 0.0249, \epsilon_l = 0.0383$
Orthorombic	6	$\begin{pmatrix} \alpha_l & \delta_l & 0 \\ \delta_l & \alpha_l & 0 \\ 0 & 0 & \beta_l \end{pmatrix}$	γ'_1 CuAlNi	$\alpha_l = 0.0425, \beta_l = -0.0822,$ $\delta_l = 0.0194$

The energy model proposed in Peigney (2023) depend on 2 main ingredients: the transformation strains $\{\boldsymbol{\tau}_j^0\}_{1 \leq j \leq n}$ of a reference crystal and the texture of the polycrystal. In the common case where the austenitic has a cubic lattice, the number n of martensitic variants and the transformation strains $\{\boldsymbol{\tau}_j^0\}_{1 \leq j \leq n}$ are determined

by the symmetry of the martensite. The most common examples are orthorhombic, monoclinic-I and monoclinic-II martensite. The corresponding values of n and $\boldsymbol{\tau}_1^0$ are reported in Table 1 along with values of the lattice parameters for some representative materials (Otsuka et al., 1971; Otsuka and Shimizu, 1974; Otsuka et al., 1974; Knowles and Smith, 1981). Only $\boldsymbol{\tau}_1^0$ is reported in Table 1: the other transformation strains are obtained from symmetries and permutation of the basis (full lists of transformation strains can be found e.g. in Bhattacharya (2003)). The tensors $\{\boldsymbol{\tau}_j^0\}_{1 \leq j \leq n}$ are symmetry related and therefore have the same eigenvalues $\lambda_1 \leq \lambda_2 \leq \lambda_3$. In a polycrystal, each crystalline orientation is characterized by a rotation \boldsymbol{r} that maps the reference basis $(\boldsymbol{u}_1, \boldsymbol{u}_2, \boldsymbol{u}_3)$ into the basis of the considered orientation. The transformation strains for the crystalline orientation \boldsymbol{r} are given by $\{\boldsymbol{r}\boldsymbol{\tau}_j^0\boldsymbol{r}^T\}_{1 \leq j \leq n}$.

A polycrystalline texture is described by a Orientation Distribution Function (ODF) $p : \text{SO}(3) \rightarrow \mathbb{R}^+$ verifying

$$1 = \int_{\boldsymbol{r} \in \text{SO}(3)} p(\boldsymbol{r}) d\mu$$

where $\text{SO}(3)$ is the group of rotations in \mathbb{R}^3 and μ is the normalized Haar measure. For later reference, we recall that the Haar measure μ enjoys the invariance property

$$\int_{\boldsymbol{r} \in \text{SO}(3)} f(\boldsymbol{r}_0 \boldsymbol{r}) d\mu = \int_{\boldsymbol{r} \in \text{SO}(3)} f(\boldsymbol{r} \boldsymbol{r}_0) d\mu = \int_{\boldsymbol{r} \in \text{SO}(3)} f(\boldsymbol{r}) d\mu \quad (6)$$

for any rotation \boldsymbol{r}_0 and any integrable function f . The expression of the Haar measure is available for common representations of rotations, such as Eulerian angles (Bunge, 2013) or axis-angle (Miles, 1965). For any set $\Gamma \subset \text{SO}(3)$, the integral $\int_{\boldsymbol{r} \in \Gamma} p(\boldsymbol{r}) d\mu$ is the fraction of crystallites whose characterizing rotations are in Γ . The ODF p can also be given a probabilistic interpretation, namely $\int_{\Gamma} p(\boldsymbol{r}) d\mu$ is the probability that the orientation of a randomly picked crystallite falls in Γ .

The energy model introduced in Peigney (2023) has the structure

$$\Psi(\boldsymbol{\varepsilon}) = \min_{\boldsymbol{\theta}} \Psi^C(\boldsymbol{\varepsilon}, \boldsymbol{\theta}) + h(\boldsymbol{\theta}). \quad (7)$$

In (7), the minimum is taken over $\boldsymbol{\theta} = (\theta_1, \dots, \theta_n)$ where the functions $\theta_j : \text{SO}(3) \mapsto [0, 1]$ verify the constraint $\sum_{j=1}^n \theta_j(\boldsymbol{r}) \leq 1$ for all $\boldsymbol{r} \in \text{SO}(3)$. The function θ_j is the (density of) volume fraction for the martensitic variant j . The function h in (7) is the so-called mixing energy (to be detailed later on) and the function Ψ^C is defined by

$$\Psi^C(\boldsymbol{\varepsilon}, \boldsymbol{\theta}) = \frac{1}{2}(\boldsymbol{\varepsilon} - \bar{\boldsymbol{\tau}}(\boldsymbol{\theta})) : \mathbb{L} : (\boldsymbol{\varepsilon} - \bar{\boldsymbol{\tau}}(\boldsymbol{\theta})) + \lambda(T) \int_{\boldsymbol{r} \in \text{SO}(3)} \sum_{j=1}^n \theta_j(\boldsymbol{r}) p(\boldsymbol{r}) d\mu \quad (8)$$

where

$$\bar{\boldsymbol{\tau}}(\boldsymbol{\theta}) = \int_{\boldsymbol{r} \in \text{SO}(3)} \sum_{j=1}^n \theta_j(\boldsymbol{r}) \boldsymbol{r} \boldsymbol{\tau}_j^0 \boldsymbol{r}^T p(\boldsymbol{r}) d\mu \quad (9)$$

can be interpreted as an effective (or average) transformation strain. In (8), \mathbb{L} is the elasticity tensor, assumed to be isotropic with a Young's modulus E and a Poisson's ratio ν . The material parameter $\lambda(T)$ is the energy of pure martensite in the stress-free state at temperature T . A commonly used expression is

$$\lambda(T) = \lambda_0 \frac{T - T_0}{T_0} \quad (10)$$

where λ_0 is the latent heat and T_0 is the transformation temperature. In this paper we consider the superelastic regime of shape memory alloys, i.e. temperatures above T_0 . Accordingly the energy term $\lambda(T)$ is assumed to be positive in the following.

Decomposition (7) with expression (8) for Ψ^C is relatively common in three-dimensional models of polycrystalline shape memory alloys (Govindjee et al., 2007; Hackl et al., 2008; Hackl and Heinen, 2008; Peigney, 2009) and assumes equal elastic moduli for all the phases. Eq. (7) implies that the stress-strain relation reads as

$$\boldsymbol{\sigma} = \mathbb{L} : (\boldsymbol{\varepsilon} - \bar{\boldsymbol{\tau}}(\boldsymbol{\theta})) \quad (11)$$

where $\boldsymbol{\theta}$ reaches the minimum in (7). Eq. (11) expresses the decomposition of the total strain $\boldsymbol{\varepsilon}$ into an elastic strain $\mathbb{L}^{-1} : \boldsymbol{\sigma}$ proportional to the stress and a transformation strain $\bar{\boldsymbol{\tau}}(\boldsymbol{\theta})$ function of the martensitic volume fractions. Micromechanical models of polycrystalline SMAs differ by the choice of the mixing energy h . The expression proposed in Peigney (2023) is

$$\begin{aligned} h(\boldsymbol{\theta}) = & \int_{\boldsymbol{r} \in \text{SO}(3)} f(\boldsymbol{\theta}(\boldsymbol{r})) p(\boldsymbol{r}) d\mu \\ & + \frac{1}{2} \int_{\boldsymbol{r} \in \text{SO}(3)} \boldsymbol{\tau}(\boldsymbol{r}) : \mathbb{L} : (\mathbb{L}^{-1} - \mathbb{P}) : \mathbb{L} : \boldsymbol{\tau}(\boldsymbol{r}) p(\boldsymbol{r}) d\mu \\ & - \frac{1}{2} \bar{\boldsymbol{\tau}}(\boldsymbol{\theta}) : \mathbb{L} : (\mathbb{L}^{-1} - \mathbb{P}) : \mathbb{L} : \bar{\boldsymbol{\tau}}(\boldsymbol{\theta}) \end{aligned} \quad (12)$$

where

$$\boldsymbol{\tau}(\boldsymbol{r}) = \sum_{j=1}^n \theta_j(\boldsymbol{r}) \boldsymbol{r} \boldsymbol{\tau}_j^0 \boldsymbol{r}^T.$$

The fourth-order \mathbb{P} tensor in (12) is the polarization tensor introduced by Willis (1977). If the orientations are isotropically distributed in space (which is assumed

from now on), then the tensor $\mathbb{L} : (\mathbb{L}^{-1} - \mathbb{P}) : \mathbb{L}$ specializes as

$$\frac{1}{2}\mathbb{L} : (\mathbb{L}^{-1} - \mathbb{P}) : \mathbb{L} = E(a\mathbb{1} \otimes \mathbb{1} + b\mathbb{I}) \quad (13)$$

where $\mathbb{1}$ and \mathbb{I} are respectively the second- and the fourth-order unit tensors, and

$$a = \frac{1 + 5\nu}{30(1 - \nu^2)}, b = \frac{7 - 5\nu}{30(1 - \nu^2)}. \quad (14)$$

The \mathbb{P} -related terms in (12) capture elastic interactions between grains, whereas the function $f : \mathbb{R}^n \mapsto \mathbb{R}$ in (12) captures intra-grain compatibility conditions. The function f is defined by a nonconvex minimization problem in \mathbb{R}^6 that generally needs to be solved numerically (see Peigney (2023) for details).

Using (3) and (11) shows that the homogeneous equilibrium states satisfy

$$\boldsymbol{\varepsilon}^* = \bar{\boldsymbol{\tau}}(\boldsymbol{\theta}^*) + (\varepsilon_{11} - \bar{\tau}_{11}(\boldsymbol{\theta}^*))(\mathbf{u}_1 \otimes \mathbf{u}_1 - \nu\mathbf{u}_2 \otimes \mathbf{u}_2 - \nu\mathbf{u}_3 \otimes \mathbf{u}_3), \quad (15)$$

$$\sigma_{11} = E(\varepsilon_{11} - \bar{\tau}_{11}(\boldsymbol{\theta}^*)) \quad (16)$$

where $\boldsymbol{\theta}^* : \text{SO}(3) \mapsto [0, 1]^n$ is a solution to the minimization problem defining $\Psi(\boldsymbol{\varepsilon}^*)$ in (7). For $\boldsymbol{\varepsilon}^*$ of the form (15), the first term in (8) reduces to $\frac{1}{2}E(\varepsilon_{11} - \bar{\tau}_{11}(\boldsymbol{\theta}^*))^2$. The densities of volume fractions $\boldsymbol{\theta}^*$ corresponding to homogeneous equilibrium states are thus obtained by solving the minimization problem

$$\min_{\boldsymbol{\theta}} \Phi(\boldsymbol{\theta}) \quad (17)$$

where

$$\Phi(\boldsymbol{\theta}) = \frac{1}{2}E(\varepsilon_{11} - \bar{\tau}_{11}(\boldsymbol{\theta}))^2 + \lambda(T) \int_{\mathbf{r} \in \text{SO}(3)} \sum_{j=1}^n \theta_j(\mathbf{r}) p(\mathbf{r}) d\mu + h(\boldsymbol{\theta}). \quad (18)$$

For any given ε_{11} , solving the minimization problem (17) for the volume fractions $\boldsymbol{\theta}^*$ and substituting the result in (15) and (16) gives the strain and stress tensors corresponding to homogeneous equilibrium states. In general, problem (17) can only be solved numerically. For simple textures with only two crystalline orientations, such numerical calculations show that the homogeneous equilibrium state can violate Hill's stability condition for ε_{11} large enough (Peigney, 2023). Common textures often involve a large number of crystalline orientations, in which case solving (17) numerically becomes quite time-consuming. This makes direct numerical calculations

impractical for performing a parametric study. In this paper, we are indeed interested in quantifying the influence of material and textural parameters on the localization phenomenon. Exploring such a of parameters by solving (17) directly would entail prohibitive calculation costs because of the many configurations to be tested. An alternative approach is adopted in the following: we consider an approximation of (17) obtained by restricting the minimization to a well-chosen set of volume fractions $\boldsymbol{\theta}$. For a large class of textures and material parameters, the approximate problem can be solved exactly, which in turn allows for a parametric study to be performed analytically. The validity of the approximate problem is assessed in Sect. 5 by comparison with the numerical solution of (17) for a selection of examples.

2.3. Approximate problem

For any given crystalline orientation \mathbf{r} , we denote by $i(\mathbf{r})$ the most favorably oriented variant with respect to the loading direction, i.e.

$$i(\mathbf{r}) = \operatorname{argmax}\{\boldsymbol{\sigma} : \mathbf{r}\boldsymbol{\tau}_j^0\mathbf{r}^T; 1 \leq j \leq n\}.$$

As noted in Sect. 2.1, the stress $\boldsymbol{\sigma}$ for homogeneous equilibrium is of the form $\sigma_{11}\mathbf{u}_1 \otimes \mathbf{u}_1$. The case of tension corresponds to $\sigma_{11} \geq 0$ (as opposed to compression). It follows that

$$i(\mathbf{r}) = \operatorname{argmax}\{\mathbf{u}_1 \cdot \mathbf{r}\boldsymbol{\tau}_j^0\mathbf{r}^T \cdot \mathbf{u}_1; 1 \leq j \leq n\}. \quad (19)$$

The corresponding transformation strain is denoted by $\boldsymbol{\eta}(\mathbf{r})$, i.e.

$$\boldsymbol{\eta}(\mathbf{r}) = \mathbf{r}\boldsymbol{\tau}_{i(\mathbf{r})}^0\mathbf{r}^T. \quad (20)$$

Numerical solutions of (17) for simple textures show that, in each grain, the most favorably oriented variant $i(\mathbf{r})$ generally dominates the other variants (Peigney, 2023). This motivates simplifying (17) by restricting the minimization to the set \mathcal{T} of functions $\boldsymbol{\theta} : \text{SO}(3) \rightarrow [0, 1]^n$ such that

$$\theta_j(\mathbf{r}) = 0 \text{ if } j \neq i(\mathbf{r}), \quad (21)$$

i.e. we consider an approximation of (17) given by the minimization problem

$$\min_{\boldsymbol{\theta} \in \mathcal{T}} \Phi(\boldsymbol{\theta}). \quad (22)$$

This approximation amounts to consider that only the most favorably variant appears in each grain. That assumption is actually commonly used in micromechanical models of polycrystalline SMAs wires and bars under tension (Nae et al., 2002; Sittner et al., 2005; Hannequart et al., 2019). For any $\boldsymbol{\theta}$ given in \mathcal{T} , the only non-zero

component of $\boldsymbol{\theta}(\mathbf{r})$ is $\theta_i(\mathbf{r})(\mathbf{r})$. That value is more simply denoted by $\theta(\mathbf{r})$ in the following, so as to alleviate the notations.

A major simplification brought by the consideration of volume fractions in \mathcal{T} is that the term $f(\boldsymbol{\theta}(\mathbf{r}))$ in (12) is known explicitly and takes the form

$$f(\boldsymbol{\theta}(\mathbf{r})) = k\theta(\mathbf{r})(1 - \theta(\mathbf{r})) \quad (23)$$

where $k/E \geq 0$ is determined (independently of \mathbf{r}) by the Poisson's ratio ν and the eigenvalues $\lambda_1 \leq \lambda_2 \leq \lambda_3$ of the transformation strains (Peigney, 2023). Eq. (23) corresponds to the solution of the two-well problem and the exact expression of k is known (Kohn, 1991). Provided that $\lambda_1 \leq -\lambda_2/2 \leq \lambda_3$ (which is notably satisfied for the examples reported in Table 1), it is shown in Peigney (2023) that k actually admits the simple expression

$$k = \frac{1}{2}E\lambda_2^2. \quad (24)$$

Use of (13) and (23) shows that $\Phi(\boldsymbol{\theta})$ can be rewritten as

$$\begin{aligned} \Phi(\boldsymbol{\theta}) = & \frac{1}{2}E(\varepsilon_{11} - \bar{\tau}_{11}(\theta))^2 + \lambda(T) \int_{\text{SO}(3)} p(\mathbf{r})\theta(\mathbf{r})d\mu + k \int_{\text{SO}(3)} p(\mathbf{r})\theta(\mathbf{r})(1 - \theta(\mathbf{r}))d\mu \\ & + E(at^2 + b\|\boldsymbol{\tau}^0\|^2) \int_{\text{SO}(3)} p(\mathbf{r})\theta^2(\mathbf{r})d\mu - E(a(\text{tr } \bar{\boldsymbol{\tau}}(\theta))^2 + b\|\bar{\boldsymbol{\tau}}(\theta)\|^2) \end{aligned} \quad (25)$$

where $t = \lambda_1 + \lambda_2 + \lambda_3$ is the trace of the transformation strains and

$$\bar{\boldsymbol{\tau}}(\theta) = \int_{\text{SO}(3)} p(\mathbf{r})\theta(\mathbf{r})\boldsymbol{\eta}(\mathbf{r})d\mu. \quad (26)$$

Normalizing Φ with respect to the Young's modulus E and setting

$$g_0 = 2(at^2 + b\|\boldsymbol{\tau}^0\|^2 - \frac{k}{E}), \quad \gamma = \frac{\lambda(T) + k}{E}, \quad (27)$$

we can rewrite $\Phi(\boldsymbol{\theta})$ as

$$\begin{aligned} \Phi(\boldsymbol{\theta}) = & \frac{1}{2}(\varepsilon_{11} - \bar{\tau}_{11}(\theta))^2 + \gamma \int_{\text{SO}(3)} p(\mathbf{r})\theta(\mathbf{r})d\mu + \frac{1}{2}g_0 \int_{\text{SO}(3)} p(\mathbf{r})\theta^2(\mathbf{r})d\mu \\ & - a(\text{tr } \bar{\boldsymbol{\tau}}(\theta))^2 - b\|\bar{\boldsymbol{\tau}}(\theta)\|^2 \end{aligned} \quad (28)$$

for any $\boldsymbol{\theta} \in \mathcal{T}$. In (27), $\|\boldsymbol{\tau}^0\|^2$ is the squared Euclidean norm of the transformation strains, i.e. $\|\boldsymbol{\tau}^0\|^2 = \lambda_1^2 + \lambda_2^2 + \lambda_3^2$. Observe from (28) that the restriction of Φ to

\mathcal{T} is quadratic. For any $\boldsymbol{\theta} \in \mathcal{T}$ and any given variation $\delta\boldsymbol{\theta} \in \mathcal{T}$, the corresponding variation $\delta\Phi$ of $\Phi(\boldsymbol{\theta})$ is given by

$$\delta\Phi = \int_{\text{SO}(3)} \Lambda(\mathbf{r}) \delta\theta(\mathbf{r}) p(\mathbf{r}) d\mu \quad (29)$$

with

$$\Lambda(\mathbf{r}) = -(\varepsilon_{11} - \bar{\tau}_{11}(\theta)) \mathbf{u}_1 \cdot \boldsymbol{\eta}(\mathbf{r}) \cdot \mathbf{u}_1 + \gamma + g_0 \theta(\mathbf{r}) - 2a(\text{tr } \bar{\boldsymbol{\tau}}(\theta)) t - 2b \bar{\boldsymbol{\tau}}(\theta) : \boldsymbol{\eta}(\mathbf{r}). \quad (30)$$

Hence the first-order local optimality condition in (22) reads as

$$\begin{cases} \Lambda(\mathbf{r}) = 0 & \text{if } 0 < \theta(\mathbf{r}) < 1 \\ \Lambda(\mathbf{r}) \geq 0 & \text{if } \theta(\mathbf{r}) = 0 \\ \Lambda(\mathbf{r}) \leq 0 & \text{if } \theta(\mathbf{r}) = 1 \end{cases} \quad (31)$$

for any \mathbf{r} such that $p(\mathbf{r}) > 0$.

Even though problem (22) or (31) is simpler than (17), it still cannot be solved analytically for any texture. An important observation is that textures commonly found in drawn wires or tubes are not arbitrary and generally show a strong $\langle 111 \rangle \parallel \mathbf{u}_1$ fiber component where \mathbf{u}_1 is along the axis of the wire or tube (Reedlunn et al., 2020). It turns out that problem (31) can be solved exactly for such textures – and more generally for textures displaying transverse isotropy along the axis of the wire/tube. This crucial point of the paper is detailed in the next section.

3. Transversely isotropic textures

We denote by \mathcal{G} the group of rotations that leave the vectorial line $\mathbb{R}\mathbf{u}_1$ invariant, i.e.

$$\mathcal{G} = \{\mathbf{r} \in \text{SO}(3) : \mathbf{r} \cdot \mathbf{u}_1 \parallel \mathbf{u}_1\}.$$

A texture is said to be *transversely isotropic* (along the direction \mathbf{u}_1) if its ODF p is invariant by \mathcal{G} , i.e. if

$$p(\mathbf{r}) = p(\mathbf{r}_0 \mathbf{r}) \text{ for all } \mathbf{r} \in \text{SO}(3), \mathbf{r}_0 \in \mathcal{G}. \quad (32)$$

Isotropic textures correspond to $p = 1$ and therefore satisfy (32). Other examples of interest are fiber textures. For given indices (n_1, n_2, n_3) , the ODF p of the fiber texture $\langle n_1 n_2 n_3 \rangle \parallel \mathbf{u}_1$ is uniformly distributed on the set $\Gamma(n_1, n_2, n_3)$ of rotations \mathbf{r} that satisfy $\mathbf{r} \cdot (n_1 \mathbf{u}_1 + n_2 \mathbf{u}_2 + n_3 \mathbf{u}_3) \parallel \mathbf{u}_1$, i.e. we have

$$p(\mathbf{r}) = \frac{\chi(\mathbf{r})}{\int_{\mathbf{r}' \in \text{SO}(3)} \chi(\mathbf{r}') d\mu} \quad (33)$$

where χ is the characteristic function of $\Gamma(n_1, n_2, n_3)$. It follows from (33) that $p(\mathbf{r}_0\mathbf{r}) = p(\mathbf{r})$ for any $\mathbf{r}_0 \in \mathcal{G}$ and $\mathbf{r} \in \text{SO}(3)$, i.e. a fiber texture $\langle n_1 n_2 n_3 \rangle \parallel \mathbf{u}_1$ is transversely isotropic along \mathbf{u}_1 . Eq. (33) correspond to a *perfect* fiber texture. In real specimen, the grains usually show some random fluctuation about the ideal orientations. That misorientation can be modeled by a random rotation \mathbf{r}_2 so that the orientation \mathbf{r} of a grain is

$$\mathbf{r} = \mathbf{r}_1\mathbf{r}_2 \quad (34)$$

where \mathbf{r}_1 follows the ideal distribution. Assuming the random variables \mathbf{r}_1 and \mathbf{r}_2 to be independent, the ODF p of the imperfect fiber texture is given by

$$p(\mathbf{r}) = \int_{\mathbf{s} \in \text{SO}(3)} p_1(\mathbf{r}\mathbf{s}^T)p_2(\mathbf{s})d\mu$$

where p_1 is the ODF of the perfect fiber texture and p_2 is the probability density of the misorientation \mathbf{r}_2 . The ODF p_1 satisfies (32) but p_2 has no reason to do so. For given rotations \mathbf{r} and \mathbf{r}_0 with $\mathbf{r}_0 \in \mathcal{G}$, we obtain

$$p(\mathbf{r}_0\mathbf{r}) = \int_{\mathbf{s} \in \text{SO}(3)} p_1(\mathbf{r}_0\mathbf{r}\mathbf{s}^T)p_2(\mathbf{s})d\mu = \int_{\mathbf{s} \in \text{SO}(3)} p_1(\mathbf{r}\mathbf{s}^T)p_2(\mathbf{s})d\mu = p(\mathbf{r})$$

It follows that $p(\mathbf{r}_0\mathbf{r}) = p(\mathbf{r})$, hence p satisfies (32).

For a transversely isotropic texture, it can be expected that the volume fractions $\boldsymbol{\theta}^*$ corresponding to homogeneous equilibrium states are also transversely isotropic, i.e. satisfy $\boldsymbol{\theta}^*(\mathbf{r}_0\mathbf{r}) = \boldsymbol{\theta}^*(\mathbf{r})$ for any $\mathbf{r}_0 \in \mathcal{G}$ and $\mathbf{r} \in \text{SO}(3)$. In that case, the tensor $\bar{\boldsymbol{\tau}}(\boldsymbol{\theta}^*)$ in (9) has the form

$$\bar{\boldsymbol{\tau}}(\boldsymbol{\theta}^*) = \bar{\tau}_{11}(\boldsymbol{\theta}^*)\mathbf{u}_1 \otimes \mathbf{u}_1 + \frac{1}{2}(\text{tr} \bar{\boldsymbol{\tau}}(\boldsymbol{\theta}^*) - \bar{\tau}_{11}(\boldsymbol{\theta}^*))(\mathbf{u}_2 \otimes \mathbf{u}_2 + \mathbf{u}_3 \otimes \mathbf{u}_3). \quad (35)$$

That relation results from the following property (proved in Appendix A):

Property 1. Let $\boldsymbol{\eta} : \text{SO}(3) \mapsto \mathbb{R}_{sym}^{3 \times 3}$ be a transversely isotropic function along \mathbf{u}_1 , i.e. such that $\boldsymbol{\eta}(\mathbf{r}_0\mathbf{r}) = \boldsymbol{\eta}(\mathbf{r})$ for all $\mathbf{r}_0 \in \mathcal{G}$. Then

$$\int_{\mathbf{r} \in \text{SO}(3)} \mathbf{r}\boldsymbol{\eta}(\mathbf{r})\mathbf{r}^T d\mu = c\mathbf{u}_1 \otimes \mathbf{u}_1 + c'(\mathbb{I} - \mathbf{u}_1 \otimes \mathbf{u}_1)$$

for some scalars c and c' .

Similar considerations apply to the approximate problem introduced in Sect. 2.3. For any transversely isotropic function $\theta : \text{SO}(3) \mapsto [0, 1]$, the tensor $\bar{\boldsymbol{\tau}}(\theta)$ in (26) can be written as

$$\bar{\boldsymbol{\tau}}(\theta) = \bar{\tau}_{11}(\theta) \mathbf{u}_1 \otimes \mathbf{u}_1 + \frac{1}{2}(\text{tr } \bar{\boldsymbol{\tau}}(\theta) - \bar{\tau}_{11}(\theta))(\mathbf{u}_2 \otimes \mathbf{u}_2 + \mathbf{u}_3 \otimes \mathbf{u}_3). \quad (36)$$

Eq. (36) follows from Property 1 and the observation that the function i in (76) is transversely isotropic along \mathbf{u}_1 . For later reference, we note from (36) that

$$a(\text{tr } \bar{\boldsymbol{\tau}}(\theta))^2 + b\|\bar{\boldsymbol{\tau}}(\theta)\|^2 = \frac{3}{2}b(\bar{\tau}_{11}(\theta))^2 + \frac{1}{2}c(\text{tr } \bar{\boldsymbol{\tau}}(\theta))^2 - b\bar{\tau}_{11}(\theta)\text{tr } \bar{\boldsymbol{\tau}}(\theta) \quad (37)$$

where $c = b + 2a$.

3.1. Parameterization of the volume fractions

Recall that any $\boldsymbol{\theta} \in \mathcal{T}$ verifies

$$\theta_j(\mathbf{r}) = \begin{cases} \theta(\mathbf{r}) & \text{if } j = i(\mathbf{r}) \\ 0 & \text{if } j \neq i(\mathbf{r}) \end{cases} \quad (38)$$

and therefore is determined by the scalar valued function θ . For an arbitrary texture, a difficulty in solving (22) is that θ is defined on $\text{SO}(3)$ and therefore is a function of 3 scalar parameters (the Euler angles). For a texture with transverse isotropy, it is natural to look for a solution θ that is also transversely isotropic and therefore depends only on 2 independent scalar parameters. We show in the following that a solution to (22) can actually be obtained from a function depending on a *single* scalar parameter. In more detail, for any given crystalline orientation \mathbf{r} , let

$$\eta(\mathbf{r}) = \mathbf{u}_1 \cdot \boldsymbol{\eta}(\mathbf{r}) \cdot \mathbf{u}_1 = \max_{1 \leq j \leq n} \mathbf{u}_1 \cdot \mathbf{r} \boldsymbol{\tau}_j^0 \mathbf{r}^T \cdot \mathbf{u}_1 \quad (39)$$

be the 11 component of the transformation strain $\boldsymbol{\eta}(\mathbf{r})$ of the most favorably oriented variant. A solution to (22) is obtained by considering volume fractions θ that only depends on \mathbf{r} through $\eta(\mathbf{r})$. Such θ can be written as

$$\theta(\mathbf{r}) = \tilde{\theta}(\eta(\mathbf{r})) \quad (40)$$

for some function $\tilde{\theta}$ defined on the set

$$I = \eta(\{\mathbf{r} \in \text{SO}(3) : p(\mathbf{r}) > 0\}) \subset \mathbb{R}^+$$

which is the set of values taken by $\eta(\mathbf{r})$ in the texture. It can easily be verified that the function η in (39) is transversely isotropic in the sense of (32), i.e. that

$\eta(\mathbf{r}) = \eta(\mathbf{r}_0\mathbf{r})$ for any $\mathbf{r}_0 \in \mathcal{G}$. Therefore, any function θ of the form (40) is also transversely isotropic.

Let $\tilde{\mathcal{T}} \subset \mathcal{T}$ be the set of functions verifying both (38) and (40). For any given $\boldsymbol{\theta} \in \tilde{\mathcal{T}}$, $\Phi(\boldsymbol{\theta})$ can be rewritten as an explicit expression in $\tilde{\theta}$. This is achieved by introducing the image measure \tilde{p} of $p\mu$ (Bogachev, 2007), defined by

$$\tilde{p}(J) = \int_{\{\mathbf{r} \in \text{SO}(3) : \eta(\mathbf{r}) \in J\}} p(\mathbf{r}) d\mu$$

for all $J \subset I$. The measure \tilde{p} has the distinctive property

$$\int_{\mathbf{r} \in \text{SO}(3)} f(\eta(\mathbf{r})) p(\mathbf{r}) d\mu = \int_{x \in I} f(x) d\tilde{p}. \quad (41)$$

where f is an arbitrary integrable function. For θ verifying (38) and (40), property (41) allows the integrals over $\text{SO}(3)$ that appear in (28) to be rewritten as integrals over the set $I \subset \mathbb{R}$. Setting

$$\bar{\eta}(\tilde{\theta}) = \int_{x \in I} x \tilde{\theta}(x) d\tilde{p}, \quad \bar{t}(\tilde{\theta}) = t \int_{x \in I} \tilde{\theta}(x) d\tilde{p}, \quad (42)$$

we obtain that $\Phi(\boldsymbol{\theta}) = \phi(\tilde{\theta})$ where

$$\phi(\tilde{\theta}) = \frac{1}{2}(\varepsilon_{11} - \bar{\eta})^2 + \gamma \int_{x \in I} \tilde{\theta}(x) d\tilde{p} + \frac{1}{2}g_0 \int_{x \in I} \tilde{\theta}^2(x) d\tilde{p} - b\frac{3}{2}\bar{\eta}^2 - \frac{1}{2}ct^2 + b\bar{t}\bar{\eta}. \quad (43)$$

In (43), the dependence of $\bar{\eta}$ and \bar{t} with respect to $\tilde{\theta}$ has been omitted in order to alleviate the notations. For any variation $\delta\tilde{\theta}$, the corresponding variation $\delta\phi$ of $\phi(\tilde{\theta})$ is equal to

$$\delta\phi = \int_{x \in I} \tilde{\Lambda}(x) \delta\tilde{\theta}(x) d\tilde{p} \quad (44)$$

with

$$\tilde{\Lambda}(x) = -(\varepsilon_{11} - \bar{\eta})x + \gamma + g_0\tilde{\theta}(x) - 3b\bar{\eta}x - ct\bar{t} + b(t\bar{\eta} + \bar{t}x). \quad (45)$$

Any $\tilde{\theta}$ minimizing ϕ in $\tilde{\mathcal{T}}$ satisfies $\delta\phi \geq 0$ for any admissible variation $\delta\tilde{\theta} \geq 0$, i.e.

$$\begin{cases} \tilde{\Lambda}(x) = 0 & \text{if } 0 < \tilde{\theta}(x) < 1 \\ \tilde{\Lambda}(x) \geq 0 & \text{if } \tilde{\theta}(x) = 0 \\ \tilde{\Lambda}(x) \leq 0 & \text{if } \tilde{\theta}(x) = 1 \end{cases} \quad (46)$$

for any $x \in I$ such that $\tilde{p}(x) > 0$.

For solving the energy minimization problem (22), a key role is played by the following

Property 2. *If $\boldsymbol{\theta} \in \tilde{\mathcal{T}}$ is such that $\delta\phi \geq 0$ for any admissible variation $\delta\tilde{\boldsymbol{\theta}}$, then $\delta\Phi \geq 0$ for any admissible variation $\delta\boldsymbol{\theta} \in \mathcal{T}$.*

Property 2 means that a local minimizer for ϕ automatically generates a local minimizer for Φ . This is interesting for our purpose because ϕ lives in a smaller space than Φ and it is therefore easier to minimize ϕ than to minimize Φ directly. We close this section with a proof of Property 2. Assume that $\boldsymbol{\theta} \in \tilde{\mathcal{T}}$ satisfies (46) and consider an arbitrary variation $\delta\boldsymbol{\theta} \in \mathcal{T}$. The corresponding variation $\delta\Phi$ is given by the general relation (29) where $\Lambda(\mathbf{r})$ is defined as in (30). Since $\boldsymbol{\theta}$ satisfies (40), $\Lambda(\mathbf{r})$ can be rewritten as

$$\Lambda(\mathbf{r}) = -(\varepsilon_{11} - \bar{\tau}_{11}(\boldsymbol{\theta}))\boldsymbol{\eta}(\mathbf{r}) + \gamma + g_0\tilde{\boldsymbol{\theta}}(\boldsymbol{\eta}(\mathbf{r})) - 2a(\text{tr } \bar{\boldsymbol{\tau}}(\boldsymbol{\theta}))t - 2b\bar{\boldsymbol{\tau}}(\boldsymbol{\theta}) : \boldsymbol{\eta}(\mathbf{r})$$

Note from (26) and (39) that

$$\bar{\tau}_{11}(\boldsymbol{\theta}) = \bar{\eta}(\tilde{\boldsymbol{\theta}}), \quad \text{tr } \bar{\boldsymbol{\tau}}(\boldsymbol{\theta}) = \bar{t}(\tilde{\boldsymbol{\theta}}), \quad (47)$$

Combining (47) with (45) gives

$$\Lambda(\mathbf{r}) = \tilde{\Lambda}(\boldsymbol{\eta}(\mathbf{r})) + b(3\bar{\eta}(\boldsymbol{\theta})\boldsymbol{\eta}(\mathbf{r}) + \bar{t}t - t\bar{\eta} - \bar{t}\boldsymbol{\eta}(\mathbf{r}) - 2\bar{\boldsymbol{\tau}}(\boldsymbol{\theta}) : \boldsymbol{\eta}(\mathbf{r})).$$

Eq. (36) yields

$$\bar{\boldsymbol{\tau}}(\boldsymbol{\theta}) : \boldsymbol{\eta}(\mathbf{r}) = \bar{\tau}_{11}(\boldsymbol{\theta})\mathbf{u}_1 \cdot \boldsymbol{\eta}(\mathbf{r}) \cdot \mathbf{u}_1 + \frac{1}{2}(\text{tr } \bar{\boldsymbol{\tau}}(\boldsymbol{\theta}) - \bar{\tau}_{11}(\boldsymbol{\theta}))(\text{tr } \boldsymbol{\tau}_{i(\mathbf{r})}^0 - \mathbf{u}_1 \cdot \boldsymbol{\eta}(\mathbf{r}) \cdot \mathbf{u}_1).$$

Recalling that $\mathbf{u}_1 \cdot \boldsymbol{\eta}(\mathbf{r}) \cdot \mathbf{u}_1 = \eta(\mathbf{r})$ and $\text{tr } \boldsymbol{\tau}_i^0 = t$, we obtain

$$\bar{\boldsymbol{\tau}}(\boldsymbol{\theta}) : \boldsymbol{\eta}(\mathbf{r}) = \frac{1}{2}(3\bar{\tau}_{11}(\boldsymbol{\theta})\eta(\mathbf{r}) + \bar{t}t - t\bar{\eta} - \bar{t}\eta(\mathbf{r})).$$

It follows that $\Lambda(\mathbf{r}) = \tilde{\Lambda}(\boldsymbol{\eta}(\mathbf{r}))$. From (40) and (46), we thus obtain that $\Lambda(\mathbf{r})$ satisfies (31), i.e. that $\delta\Phi \geq 0$ for any variation $\delta\boldsymbol{\theta} \in \mathcal{T}$. This ends the proof of Property 2.

3.2. Solution to the energy minimization problem (22)

A solution to (22) is obtained by constructing a function $\tilde{\boldsymbol{\theta}}$ that satisfies the first-order optimality conditions (46) for ϕ . It follows from Property 2 that the function $\boldsymbol{\theta}$ defined on $\text{SO}(3)$ by

$$\theta_j(\mathbf{r}) = \begin{cases} \tilde{\boldsymbol{\theta}}(\boldsymbol{\eta}(\mathbf{r})) & \text{if } j = i(\mathbf{r}) \\ 0 & \text{if } j \neq i(\mathbf{r}) \end{cases}$$

satisfies the first order optimality conditions (31), which are necessary conditions verified by solutions to the energy minimization problem (22). The functional Φ in (25) can be proved to be convex and coercive in the cases of interest (Appendix C) which ensures that the function $\boldsymbol{\theta}$ constructed is the unique solution to (22).

In the following the expressions of the solution are reported for the case where $t \geq 0$ and

$$g_0 \geq t^2 \left(c + (c - 2b(b + 3a)) \frac{(\eta^+)^2}{g_0} \right), \quad (48)$$

$$\gamma(\eta^+ - \eta^-) \leq g_0 \eta^- - bt(\langle \eta^2 \rangle - \eta^- \langle \eta \rangle). \quad (49)$$

In (49), $\eta^+ = \sup I$ and $\eta^- = \inf I$ are respectively the maximum and the minimum value taken by $\eta(\mathbf{r})$ in the texture considered. The quantities $\langle \eta \rangle$ and $\langle \eta^2 \rangle$ are respectively the average values of the transformation strain $\eta(\mathbf{r})$ and the square transformation strain $\eta^2(\mathbf{r})$ in the texture, i.e.

$$\langle \eta \rangle = \int_{\mathbf{r} \in \text{SO}(3)} \eta(\mathbf{r}) p(\mathbf{r}) d\mu, \quad \langle \eta^2 \rangle = \int_{\mathbf{r} \in \text{SO}(3)} \eta^2(\mathbf{r}) p(\mathbf{r}) d\mu.$$

Although expressions of the solution could probably be obtained in more general situations, conditions (48) and (49) are sufficient for our purpose. Let us elaborate on this point. We first note that the condition $t \geq 0$ is satisfied by common materials such as NiTi, $\gamma'_1\text{CuAlNi}$ and CuAlZn (Table 1). Condition (48) only depends through the texture through the scalar η^+ which is bounded from above by the largest eigenvalue λ_3 of the transformation strains. The most severe restriction that can arise from (48) is thus

$$g_0 \geq t^2 \left(\frac{9 + 5\nu}{30(1 - \nu^2)} + \frac{13 - 15\nu}{30(1 - \nu)^2} \frac{\lambda_3^2}{g_0} \right) \quad (50)$$

where a and b have been rewritten in terms of the Poisson's ratio ν using definition (14). For common materials, (50) is found to be satisfied to a large extent. Using the lattice parameters in Table 1, the left-hand side of (50) is indeed in the range $10^{-3} - 7 \cdot 10^{-3}$ while the right-hand side is in the range $5 \cdot 10^{-7} - 10^{-4}$.

In Condition (49), the texture appears through the various quantities η^- , η^+ , $\langle \eta \rangle$ and $\langle \eta^2 \rangle$. Let us proceed as for (48) by obtaining a sufficient condition ensuring that (49) is satisfied for any texture. Noting that $\eta(\mathbf{r})(\eta(\mathbf{r}) - \eta^-) \leq \lambda_3(\lambda_3 - \eta^-)$ and integrating over $\text{SO}(3)$, we obtain

$$\langle \eta^2 \rangle - \eta^- \langle \eta \rangle = \int_{\mathbf{r} \in \text{SO}(3)} \eta(\mathbf{r})(\eta(\mathbf{r}) - \eta^-) p(\mathbf{r}) d\mu \leq \lambda_3(\lambda_3 - \eta^-).$$

The smallest admissible value for η^- is denoted by η_{iso}^- and is achieved by a isotropic texture. A sufficient condition for (49) to be satisfied for any texture is thus

$$\gamma(\lambda_3 - \eta_{iso}^-) \leq g_0\eta_{iso}^- - bt\lambda_3(\lambda_3 - \eta_{iso}^-). \quad (51)$$

For given lattice parameters, the value η_{iso}^- can be estimated numerically. For NiTi, the maximum value of γ allowed by (51) is found to be approximately equal to $0.0017E$. Such a restriction on γ can be viewed as a restriction on the initiation stress for the austenite to martensite transformation, which is indeed equal to γ/η^+ (see Appendix B). Using the representative value $E = 45$ GPa, we obtain that Eq. (51) is satisfied in NiTi for initiation stress below 700 MPa. Tension tests from literature fulfill that condition (Churchill et al., 2009; Reedlunn et al., 2014). For γ_1' CuAlNi (resp. CuZnAl), condition (51) is satisfied for initiation stress up to 850 MPa (resp. 820 MPa).

The construction of the solution $\tilde{\theta}$ is detailed in Appendix B and here we only report the final expressions, which depend on the texture through the (positive) moment integrals

$$m_j(y) = \int_{y \leq x \leq \eta^+} x^j d\tilde{p}, \quad m^j(y) = \int_{\eta^- \leq y \leq x} x^j d\tilde{p} \quad (52)$$

for $j = 0, 1, 2$. From the integrals in (52) we can define scalar functions F and G as

$$\begin{aligned} F(y) &= \gamma \frac{g_0 + (1 - 3b)(m_2 - ym_1) + bt(m_1 - ym_0)}{g_0y - bt(m_2 - ym_1) + ct^2(m_1 - ym_0)} \\ G(y) &= (1 - 3b)\langle \eta \rangle + bt \\ &\quad + (\gamma + g_0 + bt\langle \eta \rangle - t^2c) \frac{g_0 + (1 - 3b)(m^2 - ym^1) + bt(m^1 - ym^0)}{g_0y - bt(m^2 - ym^1) + ct^2(m^1 - ym^0)} \end{aligned} \quad (53)$$

where m_j and m^j are evaluated at y . The functions F and G are monotonically decreasing (Appendix B) and we have

$$0 \leq F(\eta^+) \leq F(\eta^-) \leq G(\eta^+) \leq G(\eta^-).$$

The range of possible values for the loading parameter ε_{11} can thus be divided in the 5 intervals $[0, F(\eta^+)]$, $[F(\eta^+), F(\eta^-)]$, $[F(\eta^-), G(\eta^+)]$, $[G(\eta^+), G(\eta^-)]$, $[G(\eta^-), +\infty)$. The solution $\tilde{\theta}$ takes different expressions on those 5 intervals. More precisely,

1. If $\varepsilon_{11} \leq \gamma/\eta^+ = F(\eta^+)$ then $\tilde{\theta} = 0$. This corresponds to a fully austenitic state. This regime is labelled as *A* in the following.

2. For $F(\eta^+) \leq \varepsilon_{11} \leq F(\eta^-)$, $\tilde{\theta}$ is a piecewise linear function given by

$$\tilde{\theta}(x) = \begin{cases} 0 & \text{for } x \leq y, \\ \gamma \frac{x - y}{g_0 y - bt(m_2 - ym_1) + ct^2(m_1 - ym_0)} & \text{for } x > y \end{cases} \quad (54)$$

where y is such that $\varepsilon_{11} = f(y)$ and the functions m_j are evaluated at y . In this regime, we have $\tilde{\theta}(x) \in (0, 1)$ for all $x > y$. Hence the corresponding solution $\boldsymbol{\theta}$ to (22) is such that partial transformation between austenite and martensite takes place in the crystalline orientations \boldsymbol{r} such that $\eta(\boldsymbol{r}) > y$. The material is fully austenitic in the other crystalline orientations. This regime is labelled as $A + AM$.

3. For $F(\eta^-) < \varepsilon_{11} < G(\eta^+)$, $\tilde{\theta}$ is given by

$$\tilde{\theta}(x) = \frac{\varepsilon_{11}(x - btX_2 + ct^2X_1) - \gamma(1 + (1 - 3b)X_2 + btX_1)}{L(1, \langle \eta \rangle, \langle \eta^2 \rangle) + \langle \eta^2 \rangle - ct^2D} \quad (55)$$

where

$$\begin{aligned} L(x_0, x_1, x_2) &= g_0 - 3bx_2 + 2bt x_1 - ct^2 x_0 + \frac{2b(b + 3a)}{g_0} t^2 (x_2 x_0 - x_1^2), \\ X_i(x) &= \frac{\langle \eta^i \rangle - x \langle \eta^{i-1} \rangle}{g_0}, \quad D = \frac{\langle \eta \rangle^2 - \langle \eta^2 \rangle}{g_0}. \end{aligned} \quad (56)$$

In this regime – labelled as AM – the solution satisfies $0 < \tilde{\theta}(x) < 1$ for all $x \in I$ and corresponds to partial phase transformation in every crystalline orientation.

4. For $G(\eta^+) \leq \varepsilon_{11} \leq G(\eta^-)$, $\tilde{\theta}$ is a piecewise linear function given by

$$\tilde{\theta}(x) = \begin{cases} 1 + \frac{(\gamma + g_0 + bt \langle \eta \rangle - ct^2)(x - z)}{g_0 z - bt(m^2 - zm^1) + ct^2(m^1 - zm^0)} & \text{for } x < z, \\ 1 & \text{for } x \geq z \end{cases} \quad (57)$$

where z is such that $\varepsilon_{11} = g(z)$ and the functions m^j are evaluated at z . Eq. (57) corresponds to a state in which partial transformation takes place in the crystalline orientations \boldsymbol{r} such that $\eta(\boldsymbol{r}) < z$, the material being fully martensitic in the crystalline orientations \boldsymbol{r} such that $\eta(\boldsymbol{r}) \geq z$. This regime is labelled as $M + AM$.

5. If $\varepsilon_{11} \geq G(\eta^-)$ then $\tilde{\theta} = 1$, i.e each grain is fully transformed into its most favorable martensitic variant. This regime is labelled as M in the following.

0	A	$\bar{\eta} = 0$	
$f(\eta^+)$	$A + AM$	$\bar{\eta} = \frac{\gamma(m_2 - ym_1)}{yg_0 - bt(m_2 - ym_1) + ct^2(m_1 - ym_0)}$	with $\varepsilon_{11} = F(y)$
$f(\eta^-)$	AM	$\bar{\eta} = \frac{\varepsilon_{11}(\langle \eta^2 \rangle + ct^2 D) - \gamma \langle \eta \rangle - \gamma bt D}{L(1, \langle \eta \rangle, \langle \eta^2 \rangle) + \langle \eta^2 \rangle - ct^2 D}$	
$g(\eta^+)$	$M + AM$	$\bar{\eta} = \langle \eta \rangle + \frac{(\gamma + g_0 + bt \langle \eta \rangle - ct^2)(m^2 - zm^1)}{g_0 z - bt(m^2 - zm^1) + ct^2(m^1 - zm^0)}$	with $\varepsilon_{11} = G(z)$
$g(\eta^-)$	M	$\bar{\eta} = \langle \eta \rangle$	
ε_{11}			

Table 2: The different regimes with the corresponding expression of $\bar{\eta}$.

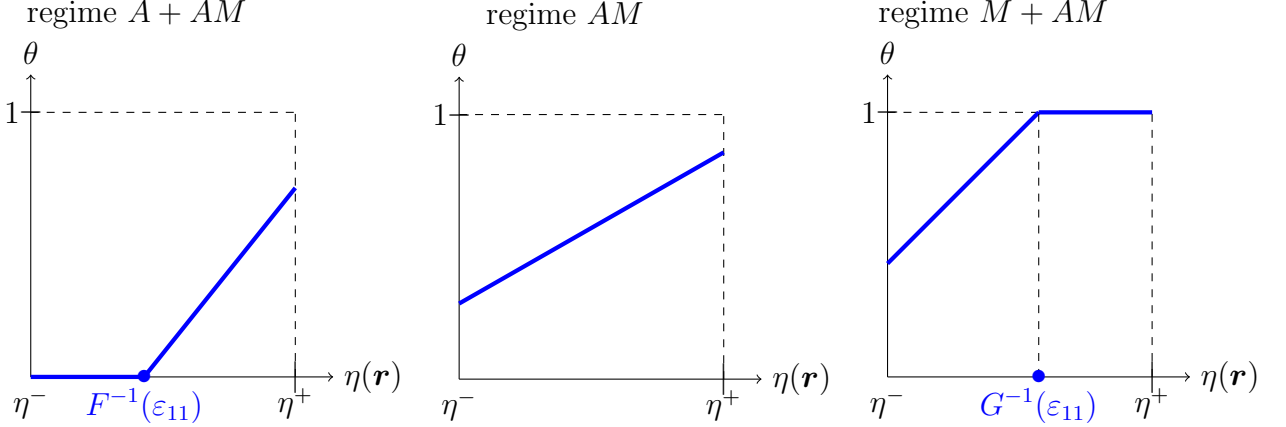


Figure 1: Plots of θ vs $\eta(\mathbf{r})$ in the three regimes $A + AM$, AM , $M + AM$.

In all cases $\tilde{\theta}$ shows a piecewise linear dependence with respect to x as represented in Fig. 1. However, the dependence of $\tilde{\theta}$ with respect to the loading parameter ε_{11} is not linear. We also note that $\tilde{\theta}$ is increasing with x , which implies that $\theta(\mathbf{r})$ in (40) is increasing with the transformation strain $\eta(\mathbf{r})$. This agrees with the intuition that martensite transformation proceeds predominantly in grains having the most favorable orientation with respect to the loading.

From the expression of $\tilde{\theta}$, one can obtain the total strain tensor $\tilde{\varepsilon}$ in (15) or the effective transformation strain tensor $\bar{\boldsymbol{\tau}}(\boldsymbol{\theta})$ in (26). For our purpose, the most relevant quantity is the effective transformation strain $\bar{\eta}$ introduced in (42). Recall indeed from (16) and (42) that

$$\sigma_{11} = E(\varepsilon_{11} - \bar{\eta}). \quad (58)$$

In Table 2 is reported the expression of $\bar{\eta}$ obtained for each of the 5 regimes. For later reference we also report the expression of \bar{t} in the $A + AM$ regime:

$$\bar{t} = \frac{\gamma t(m_1 - ym_0)}{yg_0 - bt(m_2 - ym_1) + ct^2(m_1 - ym_0)}. \quad (59)$$

The expressions in Table 2 allow one to evaluate the stress-strain relation for any transversely isotropic texture fulfilling conditions (48) and (49). As an illustrative example, consider the simple case $\tilde{p} = 1/(\eta^+ - \eta^-)$ for which the integral m_j in (52) can easily be calculated. In Fig. 2(left) is shown the stress-strain curve obtained for the values $\eta^- = 0.02$, $\eta^+ = 0.05$, $t = 0$, $\gamma = 0.0003$, $g_0 = 0.001$, $b = 0.4$. Observe in particular that the stress-strain curve is linear in all the 3 regimes A , AM and M (the corresponding parts of the stress-strain curve are highlighted in blue). That

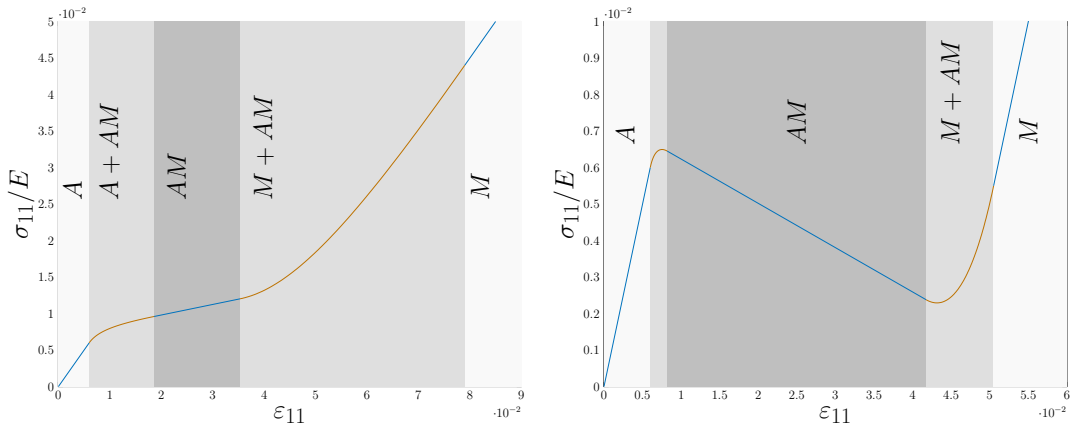


Figure 2: Stress-strain curve for a model texture with a density $\tilde{p} = 1/(\eta^+ - \eta^-)$; $\eta^+ = 0.05$, $t = 0$, $\gamma = 0.0003$, $g_0 = 0.001$, $b = 0.4$. Cases $\eta^- = 0.02$ (left) and $\eta^- = 0.04$ (right).

property actually holds for any texture and follows directly from the expression of $\bar{\eta}$ in Table 2. In Fig. 2(right) is shown the stress-strain curve obtained by increasing the value of η^- to 0.04, all the other parameters taking the same value as in Fig. 2(left). Fig. 2 illustrates two important properties of the proposed model. First, changing the texture can modify the stress-strain curve drastically. Second, for certain value of the texture parameters, the obtained stress-strain displays a softening behavior in the regime AM , meaning that instability can occur. That second property is investigated in more detail in the next section.

4. Strain localization in tension

4.1. Condition for localization

We examine conditions under which the stress-strain response obtained in Sect. 3.2 displays a negative tangent modulus $d\sigma_{11}/d\varepsilon_{11}$. From (16) and (42) we have

$$\frac{d\sigma_{11}}{d\varepsilon_{11}} = E \left(1 - \frac{d\bar{\eta}}{d\varepsilon_{11}} \right)$$

where the quantity $d\bar{\eta}/d\varepsilon_{11}$ takes different expressions depending on the value of ε_{11} . Direct calculations from the expressions in Table 2 shows that $d\sigma_{11}/d\varepsilon_{11} = E$ in regimes A and M ,

$$\frac{d\sigma_{11}}{d\varepsilon_{11}} = E \frac{L(1, \langle \eta \rangle, \langle \eta^2 \rangle)}{L(1, \langle \eta \rangle, \langle \eta^2 \rangle) + \langle \eta^2 \rangle - ct^2 D} \text{ in regime } AM. \quad (60)$$

For regime $A + AM$, we obtain from Table 2 that

$$\frac{d\sigma_{11}}{d\varepsilon_{11}} = E \left(1 - \frac{d\bar{\eta}}{dy} \frac{1}{F'(y)} \right) = E \frac{L(m_0, m_1, m_2)}{L(m_0, m_1, m_2) + m_2 - ct^2\Delta} \quad (61)$$

where $\Delta = (m_2 m_0 - m_1^2)/g_0$. In (61), the functions m_j are evaluated at the value y verifying $\varepsilon_{11} = F(y)$. In general, it is difficult to solve the equation $\varepsilon_{11} = F(y)$ in closed form and thus to express $d\sigma_{11}/d\varepsilon_{11}$ in (61) as an explicit function of ε_{11} . However, some manipulation shows that

$$\frac{d}{dy} \left(\frac{d\sigma_{11}}{d\varepsilon_{11}} \right) = Ep(y) \frac{[g_0 y - bt(m_2 - ym_1) + ct^2(m_1 - ym_0)]^2}{g_0(L(m_0, m_1, m_2) + m_2 - ct^2\Delta)^2}. \quad (62)$$

Eq. (62) implies that the tangent modulus increases with y in the regime $A + AM$. Noting from (61) that $d\sigma_{11}/d\varepsilon_{11}$ is equal to the value in (60) (resp. equal to E) when $y = \eta^-$ (resp $y = \eta^+$) and recalling that F is decreasing, we obtain

$$\frac{L(1, \langle \eta \rangle, \langle \eta^2 \rangle)}{L(1, \langle \eta \rangle, \langle \eta^2 \rangle) + \langle \eta^2 \rangle - ct^2 D} \leq \frac{1}{E} \frac{d\sigma_{11}}{d\varepsilon_{11}} \leq 1 \quad (63)$$

for any ε_{11} in $[F(\eta^+), F(\eta^-)]$. For regime $M + AM$, similar calculations show that

$$\frac{L(1, \langle \eta \rangle, \langle \eta^2 \rangle)}{L(1, \langle \eta \rangle, \langle \eta^2 \rangle) + \langle \eta^2 \rangle - ct^2 D} \leq \frac{1}{E} \frac{d\sigma_{11}}{d\varepsilon_{11}} \leq 1 \quad (64)$$

for any ε_{11} in $[G(\eta^+), G(\eta^-)]$.

Those calculations show that (60) gives the minimum value taken by $d\sigma_{11}/d\varepsilon_{11}$ along the stress-strain curve. Note that Eq. (63) implies that $L(1, \langle \eta \rangle, \langle \eta^2 \rangle, D) + \langle \eta^2 \rangle - ct^2 D \geq 0$ hence (60) has the same sign as $L(1, \langle \eta \rangle, \langle \eta^2 \rangle)$. Therefore, if $L(1, \langle \eta \rangle, \langle \eta^2 \rangle) \geq 0$ then the value in (60) is positive and the stress-strain curve shows no sign of instability. If now

$$L(1, \langle \eta \rangle, \langle \eta^2 \rangle) \leq 0 \quad (65)$$

then instability can occur. Using definition (56) of L , (65) can be rewritten as

$$g_0 - 3b\langle \eta^2 \rangle + 2bt\langle \eta \rangle - ct^2 + \frac{2b(b+3a)}{g_0} t^2 (\langle \eta^2 \rangle - \langle \eta \rangle^2) \leq 0.$$

A striking property of Condition (65) is that it depends on the texture only through the average values $\langle \eta \rangle$ and $\langle \eta^2 \rangle$.

Some results for NiTi are shown in Fig. 3 using the lattice parameters in Table 1. We consider imperfect fiber textures in which the orientation \mathbf{r} of a crystallite is given by $\mathbf{r} = \mathbf{r}_1 \mathbf{r}_2$ where \mathbf{r}_1 follows the ideal distribution of the $\langle n_1 n_2 n_3 \rangle \parallel \mathbf{u}_1$ fiber texture and \mathbf{r}_2 is a random rotation uniformly distributed on the set of rotations with angle less than a prescribed value α . Following Shu and Bhattacharya (1998), such a texture is called $\langle n_1 n_2 n_3 \rangle \parallel \mathbf{u}_1$ texture with α wobble. Let

$$X = \frac{L(1, \langle \eta \rangle, \langle \eta^2 \rangle)}{L(1, \langle \eta \rangle, \langle \eta^2 \rangle) + \langle \eta^2 \rangle - ct^2 D} \quad (66)$$

be the normalized tangent modulus in the AM regime. In Fig. 3 is shown the value taken by X in (66) as a function of α for wobbled $\langle 111 \rangle \parallel \mathbf{u}_1$, $\langle 100 \rangle \parallel \mathbf{u}_1$ and $\langle 110 \rangle \parallel \mathbf{u}_1$ textures. The average values $\langle \eta \rangle$ and $\langle \eta^2 \rangle$ are estimated numerically from a sample of 10000 random rotations \mathbf{r} distributed according to the ODF of the texture.

The solid straight line in Fig. 3 correspond to the isotropic texture: In that case, the wobble has no influence on the statistics of η so that X takes a value X_{iso} that is independent of α . For wobbled fiber textures, Fig. 3 shows that X converges towards X_{iso} as α increases. Indeed, the anisotropy of the reference perfect fiber texture gets increasingly blurred as the wobble α gets larger. In Fig. 3, the most important observation is that wobbled $\langle 111 \rangle \parallel \mathbf{u}_1$ textures fulfill the instability condition $X \leq 0$ over a wide range of wobble (approximately 0–28 °). This observation is specific to $\langle 111 \rangle \parallel \mathbf{u}_1$ textures: the other tested textures give values of X which remain relatively far above the critical line $X = 0$. We can also observe in Fig. 3 that the most critical texture (i.e. the texture that reaches the minimum value of X) is the $\langle 111 \rangle \parallel \mathbf{u}_1$ texture with approximately 15° wobble. The results in Fig. 3 have been obtained using the value $\nu = 0.3$ for the Poisson's ratio but the main conclusions are quite insensitive to the value taken by ν in the range $[0, \frac{1}{2}]$. More precisely, changing the Poisson's ratio modifies the maximum value of α for which wobbled $\langle 111 \rangle \parallel \mathbf{u}_1$ textures meet the instability condition $X \leq 0$. That maximum value increases from 27° to 29° as ν increases from 0 to $\frac{1}{2}$. None of the other considered textures is found to meet the condition $X \leq 0$, no matter the value of ν .

Results for $\gamma_1\text{CuAlNi}$ and CuZnAl are shown in Fig. 4 using a Poisson's ratio of 0.3. In contrast with NiTi, the instability condition $X \leq 0$ is never satisfied by the textures considered. Let us try to understand what is so special about $\langle 111 \rangle \parallel \mathbf{u}_1$ textures in NiTi. An important observation is that the material parameter t in NiTi— which is related to the volumetric change in the phase transformation — is relatively small compared to λ_3 . A simple approximation of the term $L(1, \langle \eta \rangle, \langle \eta^2 \rangle)$ is thus

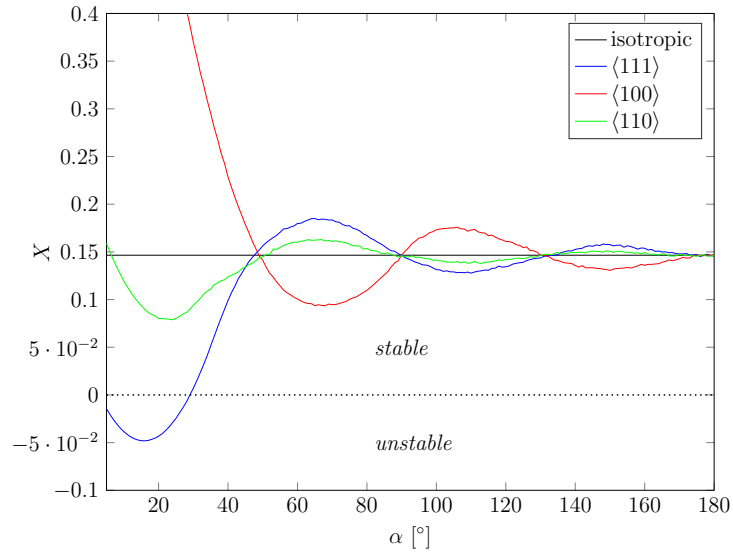


Figure 3: Localization criterion for wobbled textures in NiTi.

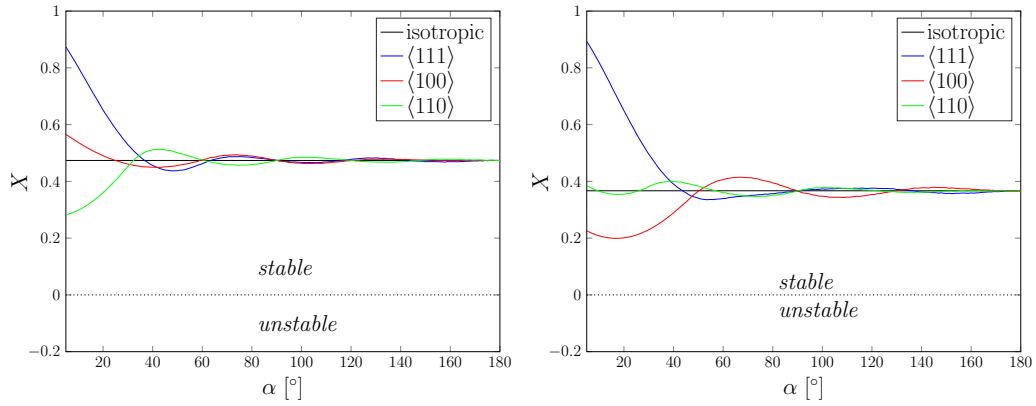


Figure 4: Localization criterion for wobbled textures in γ_1' CuAlNi (left) and CuZnAl (right).

obtained by taking $t = 0$ in (56) and (27), leading to

$$L(1, \langle \eta \rangle, \langle \eta^2 \rangle) \simeq 2b \|\boldsymbol{\tau}^0\|^2 - 2\frac{k}{E} - 3b \langle \eta^2 \rangle. \quad (67)$$

Concerning the influence of the texture on the instability condition (65), Eq. (67) shows that the dominating term is the average value $\langle \eta^2 \rangle$. In Fig. 5(left) are plotted the densities of $\eta(\mathbf{r})$ for several textures in NiTi, as estimated numerically from a sample of 100000 random rotations. Let $\eta_{iso}^- = \inf_{\mathbf{r} \in \text{SO}(3)} \eta(\mathbf{r})$ and $\eta_{iso}^+ = \sup_{\mathbf{r} \in \text{SO}(3)} \eta(\mathbf{r})$ be respectively the lowest and the largest possible value of $\eta(\mathbf{r})$ as \mathbf{r} varies as $\text{SO}(3)$. For NiTi we have $\eta_{iso}^- = \alpha_l = 0.0243$ and $\eta_{iso}^+ = \lambda_3 \simeq 0.1077$. The density corresponding to the isotropic texture (blue curve in Fig. 5) is distributed on the whole interval $[\eta_{iso}^-, \eta_{iso}^+]$, although non uniformly. By contrast, the density corresponding to fiber textures are concentrated on a small interval. Compared to other fiber textures, the density corresponding to a $\langle 111 \rangle \parallel \mathbf{u}_1$ texture has the distinctive property of being concentrated on high values of η , relatively close to the maximum achievable value $\eta_{iso}^+ = \lambda_3$. This results in high values of the average $\langle \eta^2 \rangle$, which from (67) is necessary to reach the instability condition $X \leq 0$. Increasing the wobble has the effect of spreading out the distribution of the density \tilde{p} . Let us discuss that effect in more detail in the most interesting case of $\langle 111 \rangle \parallel \mathbf{u}_1$ textures (Fig. 6). For a perfect $\langle 111 \rangle \parallel \mathbf{u}_1$ texture, it can be verified that the density \tilde{p} is a Dirac distribution concentrated at $(2\alpha_l + \beta_l + 2\delta_l + 4\epsilon_l)/3 \simeq 0.0971$. For wobble α below approximately 15° , the support $I = [\eta^-, \eta^+]$ of the density \tilde{p} extends mainly in the direction $\eta > 0$ when α increases. The net result is found to be an increase of the average value $\langle \eta^2 \rangle$. For a critical value of α approximately 15° , η^+ reaches the maximum admissible value $\eta_{iso}^+ = \lambda_3$. When α increases from that critical value, η^+ remains equal to η_{iso}^+ while η^- decreases. This is found to coincide with a decrease of the average value $\langle \eta^2 \rangle$. This evolution of \tilde{p} with α explains the down and up character of X for α around 15° (red curve in Fig. 3). The main conclusions would remain true if a gaussian random wobble was considered. In that case, the density \tilde{p} for $\langle 111 \rangle \parallel \mathbf{u}_1$ textures would cover the whole interval $[\eta_{iso}^-, \eta_{iso}^+]$ but would still remain mainly concentrated on high values of η (at least for small to moderate wobble). Similar arguments explain why $\langle 111 \rangle \parallel \mathbf{u}_1$ textures in CuZnAl give high values of X compared to the other textures: As illustrated in Fig. 5(right), the density corresponding to $\langle 111 \rangle \parallel \mathbf{u}_1$ textures in CuZnAl is concentrated on small values compared to the other textures. Also observe in Fig. 5(right) that the $\langle 100 \rangle \parallel \mathbf{u}_1$ texture in CuZnAl is in a position similar to the $\langle 111 \rangle \parallel \mathbf{u}_1$ texture in NiTi: The corresponding density is concentrated near the largest admissible value $\eta_{iso}^+ = \lambda_3$. This is the reason why $\langle 100 \rangle \parallel \mathbf{u}_1$ textures with small wobble give much smaller values of X than the

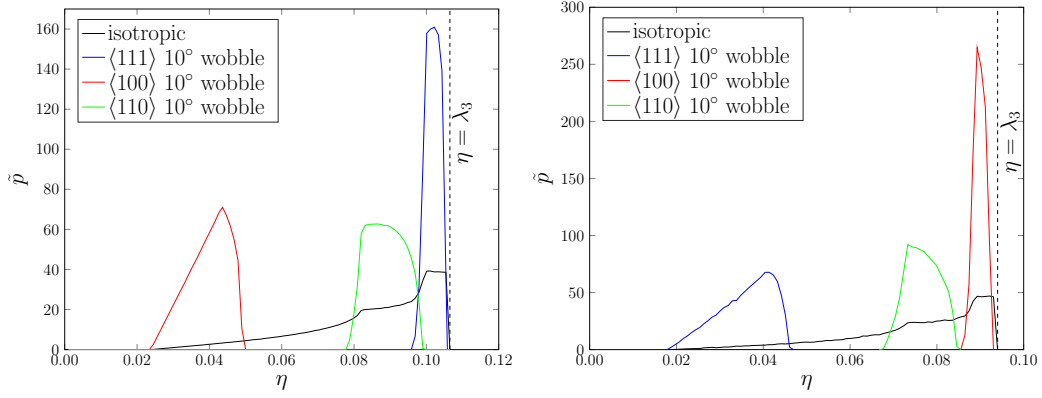


Figure 5: Densities $\tilde{\rho}$ for several textures in NiTi (left) and CuZnAl (right).

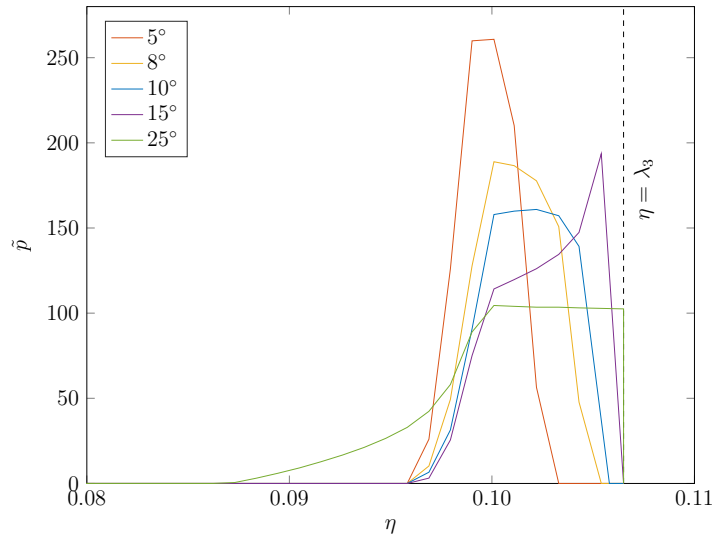


Figure 6: Densities $\tilde{\rho}$ for $\langle 111 \rangle \parallel \mathbf{u}_1$ textures with different wobble. Case of NiTi.

other textures in CuZnAl. Still the condition $X \geq 0$ is not violated in CuZnAl, as can be noted from Fig. 4(right). This is due to the values of the lattice parameters in CuZnAl, which increase the value of L compared to NiTi. More insight on the role of lattice parameters can be gained from the approximation (67). Consider the case $\langle \eta^2 \rangle = \lambda_3^2$ which is the most critical, texture-wise. Eq. (67) shows that the instability condition $X \leq 0$ is governed by the two ratios $R_1 = 2k/E\|\boldsymbol{\tau}^0\|^2$ and $R_2 = \lambda_3^2/\|\boldsymbol{\tau}^0\|^2$: those ratios need to be large enough for instability to be triggered. The ratios (R_1, R_2) are entirely determined from the lattice parameters. Using (24) shows that (R_1, R_2) can be expressed simply in terms of the eigenvalues $(\lambda_1, \lambda_2, \lambda_3)$ of the transformation strains as

$$R_1 = \frac{\lambda_2^2}{\lambda_1^2 + \lambda_2^2 + \lambda_3^2}, \quad R_2 = \frac{\lambda_3^2}{\lambda_1^2 + \lambda_2^2 + \lambda_3^2}.$$

The values taken (R_1, R_2) for NiTi, $\gamma'_1\text{CuAlNi}$ and CuAlZn are reported in Table 3. Both for R_1 and R_2 , NiTi gives larger values than the other materials. CuAlZn gives a value of R_2 that is relatively close to that of NiTi, but the value of R_1 is significantly smaller than the NiTi one. This is the reason why strain localization is not predicted for CuAlZn, even for a favorable texture. Note that R_1 and R_2 are scale-invariant quantities, so the fact that they are maximized in NiTi does not simply come from the fact that the transformation strains in NiTi are 'large'.

Table 3: Values of (R_1, R_2) in representative materials

	R_1	R_2
NiTi	0.067	0.66
CuAlZn	0.0004	0.52
$\gamma'_1\text{CuAlNi}$	0.048	0.34

4.2. Initiation stresses and peak stresses

Considering a texture meeting the instability condition $X \leq 0$. In a tensile loading starting from $\varepsilon_{11} = 0$, instability would occur at the strain $\varepsilon_{A \rightarrow M}^{peak}$ defined as the smallest value of ε_{11} for which $d\sigma_{11}/d\varepsilon_{11} \leq 0$. From the expressions of $d\sigma_{11}/d\varepsilon_{11}$ obtained in Sect. 4, the value $\varepsilon_{A \rightarrow M}^{peak}$ can be seen to necessarily fall in the regime $A + AM$. Eq. (61) shows that $\varepsilon_{A \rightarrow M}^{peak} = F(y_{A \rightarrow M}^{peak})$ where $y_{A \rightarrow M}^{peak}$ satisfies

$$L(m_0, m_1, m_2) = 0. \quad (68)$$

Note that $\varepsilon_{A \rightarrow M}^{peak}$ is strictly larger than the value $F(\eta^+)$ which from Table 2 can be interpreted as the initiation strain for the austenite to martensite transformation.

Hence in the model initiation precedes localization: at the onset of localization, transformation from austenite to martensite has already started and progressed in some grains while the others are still fully austenitic (in accordance with the definition of the $A + AM$ regime). Those theoretical results are in agreement with the experimental observations of Daly et al. (2007); Churchill et al. (2009). On the experimental stress-strain curves, a departure from linearity was indeed observed before localization. This was interpreted by the authors as a sign that phase transformation has started before localization occurs. Moreover, using digital image correlation, Daly et al. (2007) observed small fluctuations of the strain fields before localization and concluded that the transformation is heterogeneous at the microscopic scale. Related observations by Brinson et al. (2004) reported that phase transformation initiates in isolated grains. Those last observations are consistent with the definition of the $A + AM$ regime in the model.

Similar results are obtained for the reverse transformation. Decreasing the applied strain from a starting value in the M regime (see Table 2), instability would occur at the strain $\varepsilon_{M \rightarrow A}^{peak}$ defined as the largest value of ε_{11} for which $d\sigma_{11}/d\varepsilon_{11} \leq 0$. That value $\varepsilon_{M \rightarrow A}^{peak}$ falls in the regime $M + AM$ and is given by $\varepsilon_{M \rightarrow A}^{peak} = G(z_{M \rightarrow A}^{peak})$ where $z_{M \rightarrow A}^{peak}$ satisfies

$$L(m^0, m^1, m^2) = 0.$$

Let us consider a 10° wobble $\langle 111 \rangle \parallel \mathbf{u}_1$ texture, which is representative of drawn wires and tubes. In Fig. 7 is shown the stress-strain response of the material, as obtained from the expressions reported in Sect. 3.2 and using the density \tilde{p} shown in Fig. 5 (red curve). The initiation strain $\varepsilon_{A \rightarrow M}^{ini}$ is found to be approximatively equal to 0.85%. The localization strain $\varepsilon_{A \rightarrow M}^{peak}$, as obtained by solving (68), is found to be approximatively equal to 0.93%. This results in a gap $\Delta\varepsilon_{A \rightarrow M} = \varepsilon_{A \rightarrow M}^{peak} - \varepsilon_{A \rightarrow M}^{ini}$ of 0.08% which is significantly smaller than the value 0.5% observed in experiments (Churchill et al., 2009; Daly et al., 2007).

In order to assess the sensitivity of the results with respect to the wobble α , the strain gaps $\Delta\varepsilon_{A \rightarrow M}$ and $\Delta\varepsilon_{M \rightarrow A} = \varepsilon_{M \rightarrow A}^{ini} - \varepsilon_{M \rightarrow A}^{peak}$ have been evaluated for $\langle 111 \rangle \parallel \mathbf{u}_1$ textures with several levels of wobble. The obtained values are reported in Table 4. Both $\Delta\varepsilon_{A \rightarrow M}$ and $\Delta\varepsilon_{M \rightarrow A}$ are found to increase with the wobble α . However, $\Delta\varepsilon_{A \rightarrow M}$ remains significantly smaller the experimental value of 0.5%, even for exceedingly large wobble. Observe in Table 4 that $\Delta\varepsilon_{A \rightarrow M} < \Delta\varepsilon_{M \rightarrow A}$, i.e. the strain gap between localization and initiation is lower for the forward ($A \rightarrow M$) transformation than for the reverse ($M \rightarrow A$) transformation. Interestingly, this property is visible on the experimental stress-strain curve of Churchill et al. (2009).

The stress $\sigma_{A \rightarrow M}^{peak}$ (resp. $\sigma_{M \rightarrow A}^{peak}$) corresponding to the strain $\varepsilon_{A \rightarrow M}^{peak}$ (resp. $\varepsilon_{M \rightarrow A}^{peak}$) is also reported in Table 4. As will be detailed in the next section, the stresses $\sigma_{A \rightarrow M}^{peak}$

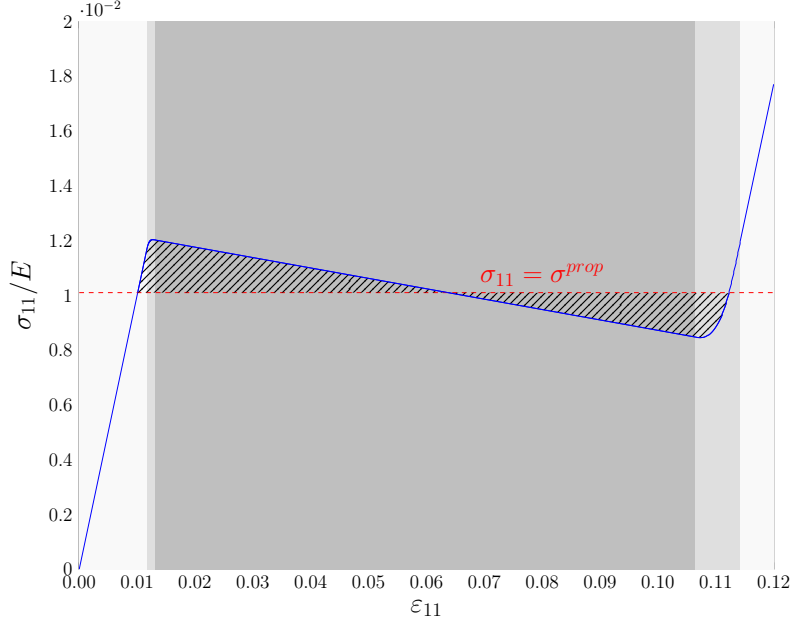


Figure 7: Stress-strain curve for the 10° wobble $\langle 111 \rangle \parallel \mathbf{u}_1$ texture. The Maxwell stress σ^{prop} is such the two hatched domains have the same area.

and $\sigma_{M \rightarrow A}^{peak}$ are related to the peak stresses that would be measured in a tensile loading-unloading cycle. The stresses $\sigma_{A \rightarrow M}^{peak}$ and $\sigma_{M \rightarrow A}^{peak}$ both vary with the wobble α and show a minimum for $\alpha \simeq 15^\circ$. The fluctuations of $\sigma_{M \rightarrow A}^{peak}$ are more pronounced than those of $\sigma_{A \rightarrow M}^{peak}$.

Table 4: Peak stresses and related results for several textures in NiTi

Texture	$\Delta \varepsilon_{A \rightarrow M}$	$\Delta \varepsilon_{M \rightarrow A}$	$\sigma_{A \rightarrow M}^{peak}/E$	$\sigma_{M \rightarrow A}^{peak}/E$	σ^{prop}/E
$\langle 111 \rangle \parallel \mathbf{u}_1$ 5° wobble	0.08%	0.49%	0.0123	0.0109	0.0115
$\langle 111 \rangle \parallel \mathbf{u}_1$ 10° wobble	0.10%	0.69%	0.0120	0.0085	0.0101
$\langle 111 \rangle \parallel \mathbf{u}_1$ 15° wobble	0.11%	0.76%	0.0119	0.0074	0.0096
$\langle 111 \rangle \parallel \mathbf{u}_1$ 20° wobble	0.13%	1.03%	0.0120	0.0080	0.0099
$\langle 111 \rangle \parallel \mathbf{u}_1$ 25° wobble	0.23%	1.60%	0.0121	0.0100	0.0110

4.3. Properties of a propagating instability

As mentioned in Sect. 2.1, some information on the bifurcated state is provided by the tensor \mathbf{d} satisfying $\mathbf{d} : (\partial^2 \Psi / \partial \varepsilon^2) : \mathbf{d} \leq 0$ at the onset of instability. In

particular, shear banding can be expected if \mathbf{d} satisfies the Hadamard compatibility conditions

$$\mathbf{d} = \mathbf{n} \otimes \mathbf{a} + \mathbf{a} \otimes \mathbf{n} \quad (69)$$

for some vectors (\mathbf{a}, \mathbf{n}) . In the present case, recall from (5), (15) and (16) that

$$\mathbf{d} = \frac{d\bar{\tau}(\boldsymbol{\theta})}{d\varepsilon_{11}} + \frac{1}{E} \frac{d\sigma_{11}}{d\varepsilon_{11}} (\mathbf{u}_1 \otimes \mathbf{u}_1 - \nu \mathbf{u}_2 \otimes \mathbf{u}_2 - \nu \mathbf{u}_3 \otimes \mathbf{u}_3).$$

At $\varepsilon_{11} = \varepsilon_{A \rightarrow M}^{peak}$, we have $d\sigma_{11}/d\varepsilon_{11} = 0$. Using the form (36) of $\bar{\tau}(\boldsymbol{\theta})$, we get

$$\mathbf{d} = \frac{d\bar{\tau}_{11}(\boldsymbol{\theta})}{d\varepsilon_{11}} \mathbf{u}_1 \otimes \mathbf{u}_1 + \frac{1}{2} \left(\frac{d\text{tr} \bar{\tau}(\boldsymbol{\theta})}{d\varepsilon_{11}} - \frac{d\bar{\tau}_{11}(\boldsymbol{\theta})}{d\varepsilon_{11}} \right) (\mathbf{u}_2 \otimes \mathbf{u}_2 + \mathbf{u}_3 \otimes \mathbf{u}_3). \quad (70)$$

Using the expression of $\boldsymbol{\theta}$ derived in Sect. 3.2, we have $\bar{\tau}_{11}(\boldsymbol{\theta}) = \bar{\eta}$ and $\text{tr} \bar{\tau}(\boldsymbol{\theta}) = \bar{t}$ where $\bar{\eta}$ and \bar{t} are expressed as functions of y in Table 2 and Eq. (59), respectively. Recalling that $\varepsilon_{11} = F(y)$, we obtain

$$\frac{d\bar{\eta}}{d\varepsilon_{11}} = \frac{1}{F'(y)} \frac{d\bar{\eta}}{dy}, \quad \frac{d\bar{t}}{d\varepsilon_{11}} = \frac{1}{F'(y)} \frac{d\bar{t}}{dy}.$$

Hence, up to multiplying constant,

$$\mathbf{d} = \frac{d\bar{\eta}}{dy} \mathbf{u}_1 \otimes \mathbf{u}_1 + \frac{1}{2} \left(\frac{d\bar{t}}{dy} - \frac{d\bar{\eta}}{dy} \right) (\mathbf{u}_2 \otimes \mathbf{u}_2 + \mathbf{u}_3 \otimes \mathbf{u}_3).$$

Carrying out the calculations of the derivatives $d\bar{\eta}/dy$ and $d\bar{t}/dy$ yields

$$\mathbf{d} = (-m_2 + (2a + b)t^2\Delta) \mathbf{u}_1 \otimes \mathbf{u}_1 + \frac{1}{2} (m_2 - tm_1 - 2at^2\Delta) (\mathbf{u}_2 \otimes \mathbf{u}_2 + \mathbf{u}_3 \otimes \mathbf{u}_3) \quad (71)$$

where $\Delta = m_0 m_2 - m_1^2$. Except for very special values of the lattice parameters, the tensor \mathbf{d} in (71) is rank-3 and therefore is not of the form (69). Hence, for wires or bars, a diffuse bifurcation mode is expected. This is consistent with the formation of necks observed in NiTi wires (Churchill et al., 2009). The situation for thin tubes is different. In that case, shear banding only requires the geometric compatibility of \mathbf{d} in the tangent plane $(\mathbf{u}_1, \mathbf{u}_\theta)$ where \mathbf{u}_θ is the orthoradial vector (Fig. 8). Denoting by $\tilde{\mathbf{d}}$ the projection of \mathbf{d} on the vectorial plane $(\mathbf{u}_1, \mathbf{u}_\theta)$, Eq. (69) is replaced by the less restrictive condition

$$\tilde{\mathbf{d}} = \mathbf{a} \otimes \mathbf{n} + \mathbf{n} \otimes \mathbf{a} \quad (72)$$

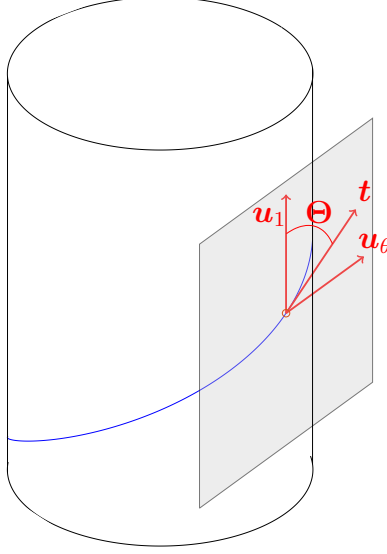


Figure 8: Localization band on a tube.

where \mathbf{n} and \mathbf{a} are vectors in the tangent plane $(\mathbf{u}_1, \mathbf{u}_\theta)$ to the tube. It can easily be verified that a given second-order tensor $\tilde{\mathbf{d}}$ defined on $(\mathbf{u}_1, \mathbf{u}_\theta)$ can be written in the form (72) iff

$$\det \tilde{\mathbf{d}} \leq 0. \quad (73)$$

If (73) is satisfied, deformation may localize in a shear band of normal \mathbf{n} on the tube. From (72), a vector \mathbf{t} in $(\mathbf{u}_1, \mathbf{u}_\theta)$ parallel to the shear band satisfies

$$\mathbf{t} \cdot \tilde{\mathbf{d}} \cdot \mathbf{t} = 0. \quad (74)$$

For the case at hand, we have

$$\tilde{\mathbf{d}} = (-m_2 + (2a + b)t^2\Delta)\mathbf{u}_1 \otimes \mathbf{u}_1 + \frac{1}{2}(m_2 - tm_1 - 2at^2\Delta)\mathbf{u}_\theta \otimes \mathbf{u}_\theta.$$

Writing \mathbf{t} as $\mathbf{t} = \cos \Theta \mathbf{u}_1 + \sin \Theta \mathbf{u}_\theta$ where Θ is the angle between the axis of the tube and the shear band, we obtain from (74) that

$$\Theta = \arctan \sqrt{\frac{2m_2 - 2(2a + b)t^2\Delta}{m_2 - tm_1 + 2at^2\Delta}}. \quad (75)$$

A perfect $\langle 111 \rangle \parallel \mathbf{u}_1$ texture in NiTi corresponds to $m_j(y) = \lambda^j H(\lambda - y)$ where $\lambda = (2\alpha_l + \beta_l + 2\delta_l + 4\epsilon_l)/3$ and H is the Heaviside function. It follows that $\Delta = 0$ so that, up to a factor λ ,

$$\tilde{\mathbf{d}} = -\lambda \mathbf{u}_1 \otimes \mathbf{u}_1 + \frac{1}{2}(\lambda - t) \mathbf{u}_\theta \otimes \mathbf{u}_\theta.$$

For NiTi (Table 1), we have $0 < t < \lambda$ hence $\det \tilde{\mathbf{d}} = -\lambda(\lambda - t) < 0$ i.e. condition (73) is satisfied. Eq. (75) gives

$$\Theta = \arctan \sqrt{\frac{2\lambda}{\lambda - t}} = \arctan \sqrt{\frac{2\alpha_l + \beta_l + 2\delta_l + 4\epsilon_l}{-2\alpha_l - \beta_l + \delta_l + 2\epsilon_l}}.$$

Using the values of the lattice parameters in Table 1 gives $\Theta \sim 55.4^\circ$. For wobbled $\langle 111 \rangle \parallel \mathbf{u}_1$ textures, numerical calculations show that (73) is satisfied for all wobbles satisfying the instability condition. The angle Θ predicted by (75) shows very little variation ($< 0.1^\circ$) with the wobble. We note that the predicted angle of 55.4° is close to the experimental observations, which give an angle Θ in the range $55 - 61^\circ$ (Sun and Li, 2002; Reedlunn et al., 2014, 2020).

Once the instability is formed, its propagation stress σ^{prop} can be estimated using Maxwell's equal area rule (Ericksen, 1975): in the $\varepsilon_{11} - \sigma_{11}$ plane, the line $\sigma_{11} = \sigma^{prop}$ intersects the stress-strain curve $\sigma_{11} = \mathcal{F}(\varepsilon_{11})$ at three values $\varepsilon_a \leq \varepsilon_b \leq \varepsilon_c$ such that the domains

$$\{(\varepsilon_{11}, \sigma_{11}) : \varepsilon_a \leq \varepsilon_{11} \leq \varepsilon_b, \sigma^{prop} \leq \sigma_{11} \leq \mathcal{F}(\varepsilon_{11})\}$$

and

$$\{(\varepsilon_{11}, \sigma_{11}) : \varepsilon_b \leq \varepsilon_{11} \leq \varepsilon_c, \mathcal{F}(\varepsilon_{11}) \leq \sigma_{11} \leq \sigma^{prop}\}$$

have the same area, as represented in Fig. 7. The obtained values for σ^{prop} are reported in Table 4 for $\langle 111 \rangle \parallel \mathbf{u}_1$ textures with several levels of wobble. For a tensile loading starting from 0, a sudden stress drop from $\sigma_{A \rightarrow M}^{peak}$ to σ^{prop} is thus expected when the applied strain crosses the critical value $\sigma_{A \rightarrow M}^{peak}$. For a $\langle 111 \rangle \parallel \mathbf{u}_1$ texture with 10° wobble, the theoretical value of the ratio $(\sigma_{A \rightarrow M}^{peak} - \sigma^{prop})/\sigma^{prop}$ is equal to 0.19. Using the representative value $E = 45000$ GPa for the Young's modulus, this corresponds to a stress drop $\sigma_{A \rightarrow M}^{peak} - \sigma^{prop}$ of 85 MPa, which is of the same order as the experimental value of 94 MPa reported by Churchill et al. (2009).

4.4. Compression

Adapting the presented analysis to strain-driven compression is simply achieved by changing the definition (76) of the most favorably oriented variant $i(\mathbf{r})$, which becomes

$$i(\mathbf{r}) = \operatorname{argmin}\{\mathbf{u}_1 \cdot \mathbf{r} \tau_j^0 \mathbf{r}^T \cdot \mathbf{u}_1; 1 \leq j \leq n\}. \quad (76)$$

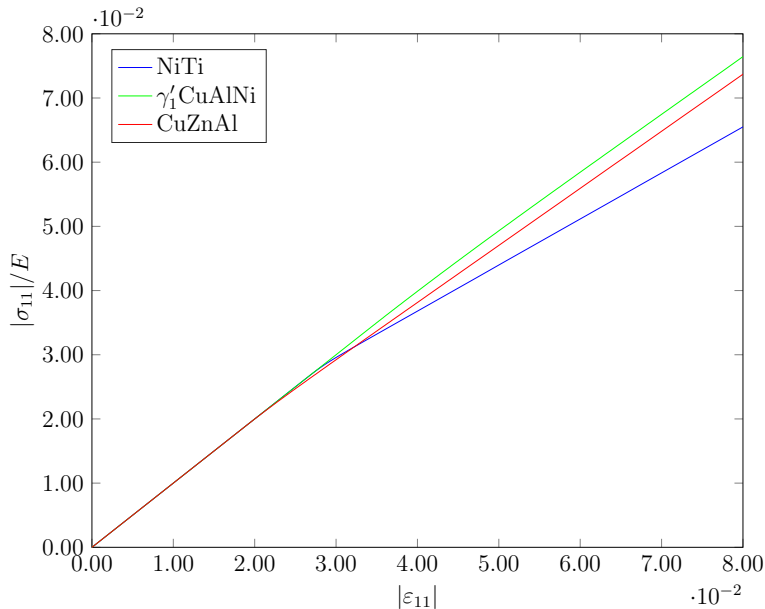


Figure 9: Compressive stress-strain curves for several materials with a fiber texture $\langle 111 \rangle \parallel \mathbf{u}_1$.

for compression. The most favorably variants with respect to tension and compression are not the same, which results in different values for the averages $\langle \eta^2 \rangle$ and more generally for the density function \tilde{p} of the transformation strain $\eta(\mathbf{r})$. In Fig. 9 are shown the stress-strain curves obtained for compression in NiTi, γ'_1 CuAlNi and CuZnAl. Those curves are obtained from the expressions in Table 2, assuming a $\langle 111 \rangle \parallel \mathbf{u}_1$ fiber texture with 10° wobble. There is no sign of instability in Fig. 9 as the tangent modulus remains positive along all the three curves. Changing the wobble α does not modify that conclusion, as illustrated in Fig. 10(left) showing the quantity X in (66) as a function of α . In contrast with the tension case, the instability condition $X \leq 0$ is never met, whatever the value of α . This behavior is directly connected to the density \tilde{p} of the transformation strain $\eta(\mathbf{r})$, which for compression can be verified to be concentrated on small values, as illustrated in Fig. 10(right).

5. Comparison with numerical simulations

5.1. Influence of the number of grains

The transverse isotropy of the texture is a key ingredient for solving problem (22) in closed form. In practice, polycrystalline textures involve a finite number N

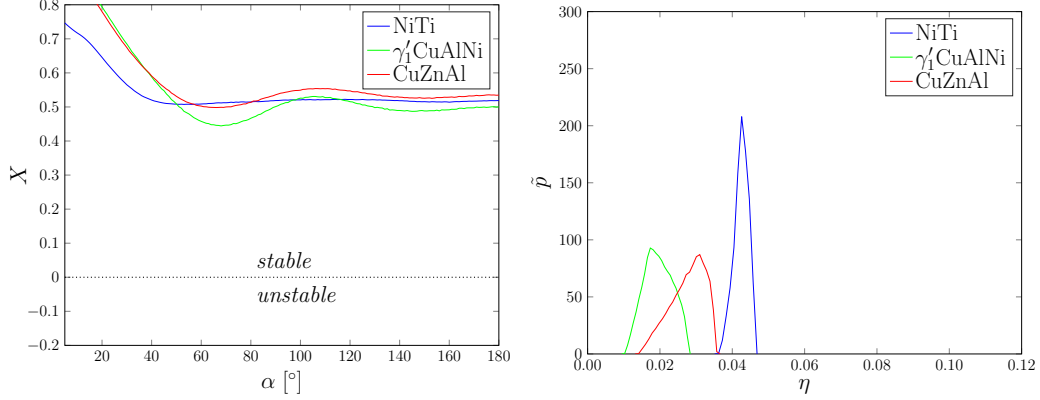


Figure 10: (left) Localization criterion vs wobble for a fiber texture $\langle 111 \rangle \parallel \mathbf{u}_1$ in several materials. (right) Densities of the transformation strain η for a fiber texture $\langle 111 \rangle \parallel \mathbf{u}_1$ (with 10° wobble) in several materials.

of grains so that transverse isotropy is only respected up to some approximation. For a texture with a finite number of grains, the problem to be solved is a special case of (22) where both p and θ are sums of Dirac masses. In more detail, the ODF p corresponding to a texture with N grains can be written as

$$p = \sum_{j=1}^N p_j \delta_{\mathbf{r}^j} \quad (77)$$

where \mathbf{r}^j is the orientation in grain j and $\delta_{\mathbf{r}^j}$ is the Dirac mass at \mathbf{r}^j (verifying $\int_{\text{SO}(3)} f(\mathbf{r}) \delta_{\mathbf{r}^j} d\mu = f(\mathbf{r}^j)$ for any integrable function f on $\text{SO}(3)$). The weights p_j in (77) correspond to the volume fractions of the grains: they are positive and satisfy $\sum_j p_j = 1$. The function Φ in (28) specializes as

$$\Phi(\theta_1 \cdots, \theta_N) = \frac{1}{2} (\varepsilon_{11} - \bar{\tau}_{11}(\boldsymbol{\theta}))^2 + \gamma \sum_{j=1}^N p_j \theta_j + \frac{1}{2} g_0 \sum_{j=1}^N p_j \theta_j^2 - a (\text{tr } \bar{\boldsymbol{\tau}}(\boldsymbol{\theta}))^2 - b \|\bar{\boldsymbol{\tau}}(\boldsymbol{\theta})\|^2 \quad (78)$$

where

$$\bar{\boldsymbol{\tau}}(\boldsymbol{\theta}) = \sum_{j=1}^N p_j \theta_j \mathbf{r}^j \boldsymbol{\tau}^i(\mathbf{r}^j) \mathbf{r}^{j,T}$$

and θ_j is the volume fraction of the most favorably oriented variant in grain j . The volume fractions $\theta_1 \cdots, \theta_N$ are obtained by solving the minimization problem

$$\min_{(\theta_1 \cdots, \theta_N) \in [0,1]^N} \Phi(\theta_1 \cdots, \theta_N). \quad (79)$$

The stress σ_{11} directly follows from the solution of (79) via the relation $\sigma_{11} = E(\varepsilon_{11} - \bar{\tau}_{11}(\boldsymbol{\theta}))$.

We wish to compare the analytical solution presented in Sect. 3.2 with numerical solutions obtained for a finite number N of grains. Let us consider the case of a $\langle 111 \rangle \parallel \mathbf{u}_1$ textures with 10° wobble. Textures with $N = 100$ grains are generated by taking $p_j = 1/N$ in (77). The orientations \mathbf{r}^j are generated by writing \mathbf{r}^j as $\mathbf{r}^j = \mathbf{r}_1^j \mathbf{r}_2^j$ where \mathbf{r}_1^j is chosen randomly (with a uniform distribution) in the set of rotations having a angle lower than 10° and \mathbf{r}_2^j is chosen randomly (with a uniform distribution) in the set of rotations such that $\mathbf{r}_2^j(\mathbf{u}_1 + \mathbf{u}_2 + \mathbf{u}_3) \parallel \mathbf{u}_1$. The quadratic programming problem (79) was solved numerically using an interior-point algorithm (Ye, 2011). In Fig. 11 are shown some stress-strain curves calculated for 10 of such 100-grains aggregates. Due to randomness, there is some variability in the stress-strain curves obtained. We choose to evaluate the difference between the response of a 100-grain polycrystal and the analytical solution of Sect. 3.2 by comparing the lowest value taken by the tangent modulus, which is indeed the quantity driving strain localization in the present study. The lowest tangent modulus is equal to X in (66) for the analytical solution and its value for a 100-grain aggregate is denoted by X_{100} . In Fig. 12 is shown an histogram of the relative difference $(X - X_{100})/X$ as obtained from a sample of 1000 polycrystals of 100 grains. The average value of $(X - X_{100})/X$ is approximatively 2.2% and the relative standard deviation is about 6%. Those results show that the analytical solution presented in Sect. 3.2 gives a good statistical estimate of the response of 100-grain polycrystals. The accuracy improves with the number of grains: The average value of the relative difference drops to 1.4% (resp. 0.7%) for polycrystals with 200 grains (resp. 500 grains).

For a polycrystal with a finite number of grains, the fact that transverse isotropy is not respected exactly also has an influence on the inclination predicted for the shear bands. Although it is no longer of the form (70), the tensor \mathbf{d} at the onset of localization is still found to satisfy the condition (72) corresponding to shear banding on a thin-walled tube. The angle Θ of the band, however, now depends on the angular coordinate on the tube. Let Θ_{min} and Θ_{max} be respectively the minimum and the maximum value taken by Θ as the angular coordinate varies between 0 and 2π . Averaging Θ_{min} and Θ_{max} over 1000 polycrystals of 100 grains gives values of 55.0° and 55.9° respectively, which remains close to the theoretical value of 55.4° obtained in Sect. 3.2 under the assumption of transverse isotropy.

5.2. Influence of the number of active variants per orientation

The analytical results presented so far lie on the approximation that only the most favorably oriented variant appears in each grain. That approximation has the

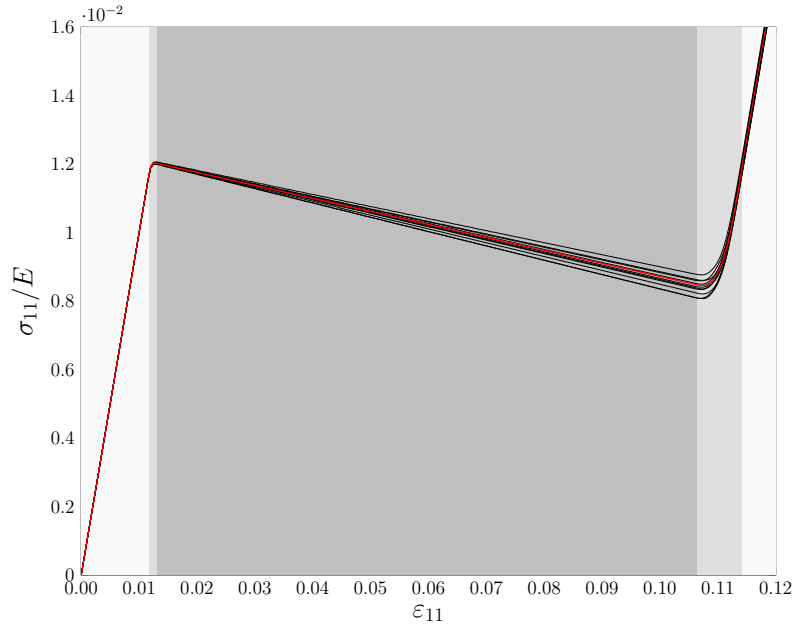


Figure 11: stress-strain curves for $\langle 111 \rangle \parallel \mathbf{u}_1$ textures with 10° wobble: numerical solutions for examples of textures with 100 grains (black), analytical solution (red).

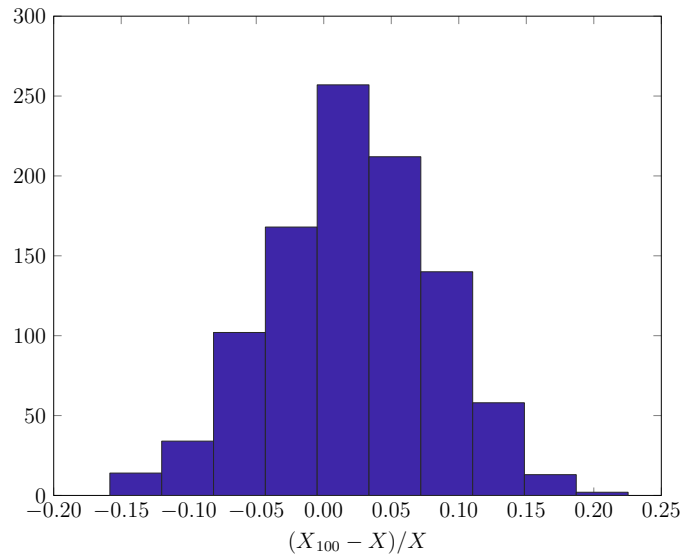


Figure 12: Histogram of the relative difference $(X - X_{100})/X$ for a sample of 1000 polycrystals. Each polycrystal has 100 randomly generated crystalline orientations.

downside of giving too much weight to the mixing energy h in (25). In reality, distributing the martensitic volume fraction on the top 2 (or more) most favorably oriented variants in each grain may significantly reduce the mixing energy without impacting significantly the quadratic term $\frac{1}{2}E(\varepsilon_{11} - \bar{\tau}_{11}(\boldsymbol{\theta}))^2$ that captures the loading orientation in (25). In this section we are interested in investigating how the results are impacted when several variants are taken into account. In that case, it is no longer possible to obtain analytical solutions and the energy minimization problem needs to be solved numerically. We consider 100-grain polycrystals with textures generated using the same process as in Sect. 5.1 and the minimization problem (25) was solved numerically. The obtained value of Φ , denoted by Φ_{num} , is necessarily smaller than the value Φ_{ana} corresponding to the results of Sect. 5.1 because the minimization is carried out over a larger set of volume fractions.

Tensile stress-strain curves are shown in Figs. 13–15 for three representative materials: $\langle 111 \rangle \parallel \mathbf{u}_1$ texture (with 10° wobble) in NiTi, isotropic texture in NiTi, $\langle 111 \rangle \parallel \mathbf{u}_1$ texture (with 10° wobble) in γ'_1 CuAlNi. The red curves are the numerical results obtained for 100-grain polycrystals. Shown in blue are the analytical stress-strain curves obtained from the results of Sect 3.2. A first observation is that the numerical simulations overall give lower values for the stress. This is consistent with the fact that $\Phi_{num} < \Phi_{ana}$. The energies $\Phi_{num}(\varepsilon_{11})$ and $\Phi_{ana}(\varepsilon_{11})$ are indeed the areas under the stress-strain curves in Figs. 13–15. Interestingly, the red curve in Fig. 13 shows some similarity to the underlying material response extracted by Hallai and Kyriakides (2013) from tension tests on NiTi laminates.

Even though details of the stress-strain curves are different, an important observation is that the approximate model studied in Sect.3.2 does a good job of capturing the minimum tangent modulus, which is the key quantity for predicting strain localization in the present study. This builds confidence in the analytical results of Sect. 4 for accurately predict localization. However, in cases where strain localization is expected, taking several variants into account does impact quantities such as the peak stress and the propagation stress. Let us detail those effects for the $\langle 111 \rangle \parallel \mathbf{u}_1$ texture in NiTi. For the $A \rightarrow M$ transformation, the numerical simulations give an initiation strain of 0.9% (corresponding to a stress of 400 MPa) and a localization strain $\varepsilon_{A \rightarrow M}^{peak}$ of 1.6%. The strain gap $\Delta\varepsilon_{M \rightarrow A} = \varepsilon_{M \rightarrow A}^{ini} - \varepsilon_{M \rightarrow A}^{peak}$ is thus equal to 0.7%, which is significantly larger than the value obtained in Sect. 4.2) (0.08%) and closer to the experimental value (0.5%) reported by Churchill et al. (2009). For the $M \rightarrow A$ transformation, the strain gap $\Delta\varepsilon_{M \rightarrow A}$ between initiation and localization is about 2%, which again is larger than the value obtained previously in Sect. 4.2. Note that we still have $\Delta\varepsilon_{M \rightarrow A} > \Delta\varepsilon_{A \rightarrow M}$ from the simulations, as already observed in Sect. 4.2 and consistently with the experiments.

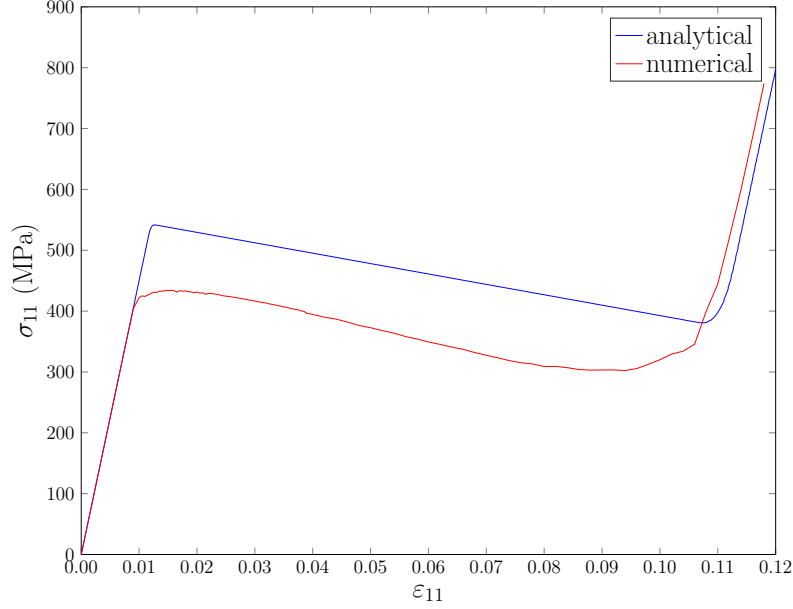


Figure 13: stress-strain curves for $\langle 111 \rangle \parallel \mathbf{u}_1$ textures with 10° wobble: numerical solutions for a texture with 100 grains (red), analytical approximation (blue).

The numerical simulations give a stress peak $\varepsilon_{M \rightarrow A}^{peak}$ of 435 MPa for the $A \rightarrow M$ transformation and the Maxwell stress σ^{prop} is about 370 MPa. The resulting stress drop at localization is thus 65 MPa, which is smaller than the experimental values reported by Churchill et al. (2009) (94 MPa for the $A \rightarrow M$ transformation and 77 MPa for the $M \rightarrow A$ transformation) even though the order of magnitude is correct. At the onset of localization, the tensor \mathbf{d} obtained from the numerical simulations is

$$\begin{pmatrix} 0.5068 & 0.0120 & -0.0065 \\ 0.0120 & -0.2416 & 0.0138 \\ -0.0065 & 0.0138 & -0.2363 \end{pmatrix}$$

That tensor satisfies the condition 73 for shear banding on a tube. The inclination of the band is found to be in the range $54.8 - 56.3^\circ$ depending on the location on the tube.

6. Concluding remarks

The central relation (65) show that instability under tension is deeply connected to the lattice parameters and the statistics of the transformation strain. Among

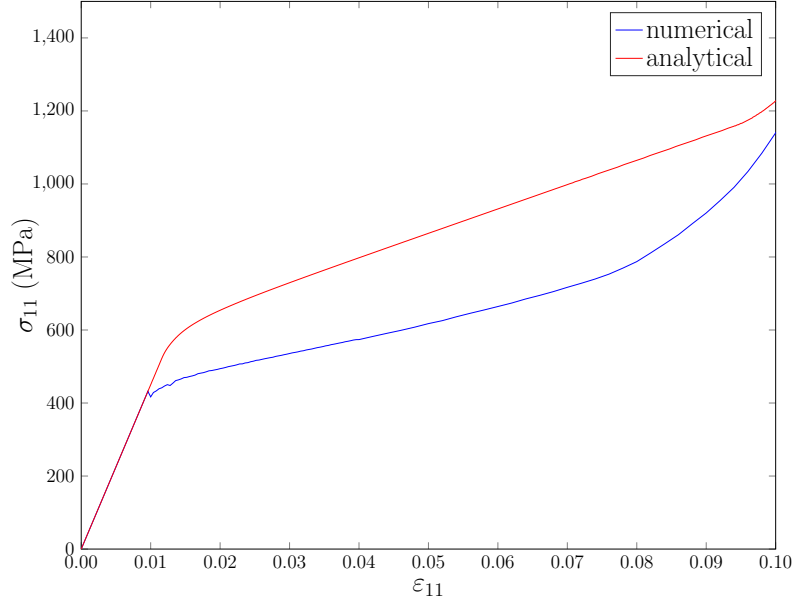


Figure 14: stress-strain curves for an isotropic texture in NiTi: numerical solutions for 100 grains (red), analytical approximation (blue).

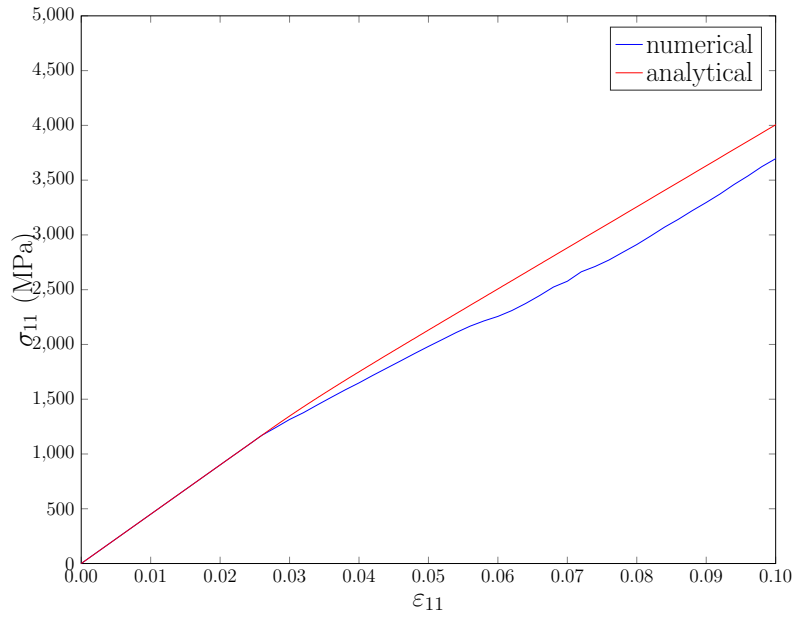


Figure 15: stress-strain curves for a $\langle 111 \rangle \parallel \mathbf{u}_1$ texture with 10° wobble in CuAlNi: numerical solutions for 100 grains (red), analytical approximation (blue).

common polycrystalline materials, NiTi is found to be the only one fulfilling the necessary conditions for strain localization to occur. This is due to the combined effect of the $\langle 111 \rangle \parallel \mathbf{u}_1$ texture (which results in large values of $\langle \eta^2 \rangle$) and the transformation strains in NiTi (which achieve large values of $\lambda_2^2 / \|\boldsymbol{\tau}_0\|^2$). The results obtained are complementary to those of Sittner et al. (2005) and point in the same direction. In the work of Sittner et al. (2005), strain localization is interpreted as a *geometric* instability and the influence of elastic anisotropy is emphasized. In the present study, strain localization is interpreted a *material* instability and the influence of austenite-martensite compatibility is highlighted. In both approaches, texture effects and transformation anisotropy play a crucial role in strain localization. As advanced by Daly et al. (2007), strain localization is most probably an interplay between geometric and material instability, so it would be interesting to combine the two approaches. One step in that direction would be to extend the energy model used in this paper to take elastic anisotropy into account. An other line of investigation consists in studying more complex loadings for which strain localization in tubes has been reported experimentally, such as bending (Bechle and Kyriakides, 2014; Reedlunn et al., 2014), combined torsion-traction (Reedlunn et al., 2020) or combined traction-pressure (Bechle and Kyriakides, 2016). The tailoring of lattice parameters to achieve (or avoid) specific macroscopic behavior is receiving increasing attention in recent research on SMAs. In that regard, the results presented in this paper could be used to investigate the range of lattice parameters in monoclinic-I martensite for which the stability condition is satisfied over a reasonable range of wobble amplitude α .

Appendix A. Proof of Property 1

Let

$$\bar{\boldsymbol{\eta}} = \int_{\mathbf{r} \in \text{SO}(3)} \mathbf{r} \boldsymbol{\eta}(\mathbf{r}) \mathbf{r}^T d\mu$$

where $\boldsymbol{\eta} : \text{SO}(3) \mapsto \mathbb{R}_{sym}^{3 \times 3}$ is such that $\boldsymbol{\eta}(\mathbf{r}_0 \mathbf{r}) = \boldsymbol{\eta}(\mathbf{r})$ for all $\mathbf{r}_0 \in \mathcal{G}$. For any $\mathbf{r}_0 \in \mathcal{G}$, we have

$$\mathbf{r}_0 \bar{\boldsymbol{\eta}} \mathbf{r}_0^T = \int_{\mathbf{r} \in \text{SO}(3)} (\mathbf{r}_0 \mathbf{r}) \boldsymbol{\eta}(\mathbf{r}) (\mathbf{r}_0 \mathbf{r})^T d\mu$$

which using (6) can be rewritten as

$$\mathbf{r}_0 \bar{\boldsymbol{\eta}} \mathbf{r}_0^T = \int_{\mathbf{r} \in \text{SO}(3)} \mathbf{r} \boldsymbol{\eta}(\mathbf{r}_0^T \mathbf{r}) \mathbf{r}^T d\mu. \quad (\text{A.1})$$

Since $\boldsymbol{\eta}$ is transversely isotropic, the right-hand side of (A.1) is equal to $\bar{\boldsymbol{\eta}}$. We have thus established that $\mathbf{r}_0 \bar{\boldsymbol{\eta}} \mathbf{r}_0^T = \bar{\boldsymbol{\eta}}$ i.e. that

$$\mathbf{u} \cdot \mathbf{r}_0 \bar{\boldsymbol{\eta}} \mathbf{r}_0^T \cdot \mathbf{v} = \mathbf{u} \cdot \bar{\boldsymbol{\eta}} \cdot \mathbf{v} \quad (\text{A.2})$$

for any vectors (\mathbf{u}, \mathbf{v}) . Choose \mathbf{r}_0 as the rotation with axis \mathbf{u}_1 and angle π . Using (A.2) with $(\mathbf{u}, \mathbf{v}) = (\mathbf{u}_1, \mathbf{u}_2)$ shows that $\mathbf{u}_1 \cdot \bar{\boldsymbol{\eta}} \cdot \mathbf{u}_2 = 0$. Similarly, using (A.2) with $(\mathbf{u}, \mathbf{v}) = (\mathbf{u}_1, \mathbf{u}_3)$ shows that $\mathbf{u}_1 \cdot \bar{\boldsymbol{\eta}} \cdot \mathbf{u}_3 = 0$. Now choose \mathbf{r}_0 as the rotation with axis \mathbf{u}_1 and angle $\pi/2$, so that $\mathbf{r}_0 \cdot \mathbf{u}_2 = \mathbf{u}_3$ and $\mathbf{r}_0 \cdot \mathbf{u}_3 = -\mathbf{u}_2$. Using (A.2) with $(\mathbf{u}, \mathbf{v}) = (\mathbf{u}_2, \mathbf{u}_3)$ shows that $\mathbf{u}_2 \cdot \bar{\boldsymbol{\eta}} \cdot \mathbf{u}_3 = -\mathbf{u}_3 \cdot \bar{\boldsymbol{\eta}} \cdot \mathbf{u}_2$. Finally using (A.2) with $(\mathbf{u}, \mathbf{v}) = (\mathbf{u}_2, \mathbf{u}_2)$ gives $\mathbf{u}_2 \cdot \bar{\boldsymbol{\eta}} \cdot \mathbf{u}_2 = \mathbf{u}_3 \cdot \bar{\boldsymbol{\eta}} \cdot \mathbf{u}_3$. Noting that $\bar{\boldsymbol{\eta}}$ is symmetric, we finally arrive at $\bar{\boldsymbol{\eta}} = c\mathbf{u}_1 \otimes \mathbf{u}_1 + c'(\mathbf{u}_2 \otimes \mathbf{u}_2 + \mathbf{u}_3 \otimes \mathbf{u}_3)$ for some scalars (c, c') , which is the desired result.

Appendix B. Solution of (46) for transversely isotropic textures

Appendix B.1. Regime A

Let us first examine the possibility that $\tilde{\theta} = 0$ is a solution to (46). Recalling that $\eta^+ = \sup I$, we obtain from (46) that the condition for $\tilde{\theta} = 0$ to be a solution is

$$\varepsilon_{11} \leq \frac{\gamma}{\eta^+}. \quad (\text{B.1})$$

Appendix B.2. Regime A + AM

When ε_{11} exceeds γ/η^+ , the function $\tilde{\theta} = 0$ first violates condition (46) at $x = \eta^+$. For a certain range of strain ε_{11} above γ/η^+ , we thus expect a solution to (46) to be such that

$$\begin{aligned} \tilde{\theta}(x) &= 0 & \text{for } \eta^- \leq x \leq y \\ \tilde{\theta}(x) &\in (0, 1) & \text{for } y < x \leq \eta^+ \end{aligned} \quad (\text{B.2})$$

where $y \in I$ is to be determined as a function of the applied strain ε_{11} . For $\tilde{\theta}$ of the form (B.2), the optimality condition (46) reads as

$$\begin{aligned} 0 &\leq -(\varepsilon_{11} - (1 - 3b)\bar{\eta})x + \gamma - ct\bar{t} + b(t\bar{\eta} + \bar{t}x) & \text{for } x \leq y, \\ 0 &= -(\varepsilon_{11} - (1 - 3b)\bar{\eta})x + \gamma - ct\bar{t} + b(t\bar{\eta} + \bar{t}x) + g_0\tilde{\theta}(x) & \text{for } x > y. \end{aligned} \quad (\text{B.3})$$

We look for a solution $\tilde{\theta}$ that is continuous at y , so that taking the limit $x \rightarrow y$ in the second equation in (B.3) gives

$$0 = -(\varepsilon_{11} - (1 - 3b)\bar{\eta})y + \gamma - ct\bar{t} + b(t\bar{\eta} + \bar{t}y). \quad (\text{B.4})$$

The exact expression of $\tilde{\theta}(x)$ can be obtained from (B.3) and (B.4) as detailed in the following. Integrating the second equation in (B.3) over the interval $[y, \eta^+]$ yields

$$0 = -(\varepsilon_{11} - (1 - 3b)\bar{\eta})m_1 + \gamma m_0 - c\bar{t}m_0 + b(t\bar{\eta}m_0 + \bar{t}m_1) + g_0 \int_y^{\eta^+} \tilde{\theta} d\tilde{p} \quad (\text{B.5})$$

where m_j is the integral introduced in (52), evaluated at y . Multiplying the second equation in (B.3) by x and integrating over the interval $[y, \eta^+]$, we obtain

$$0 = -(\varepsilon_{11} - (1 - 3b)\bar{\eta})m_2 + \gamma m_1 - c\bar{t}m_1 + b(t\bar{\eta}m_1 + \bar{t}m_2) + g_0 \int_y^{\eta^+} x\tilde{\theta}(x)d\tilde{p}. \quad (\text{B.6})$$

Since the function $\tilde{\theta}$ in (B.2) vanishes for $x \leq y$, the integrals in the right-hand side of (B.5) and (B.6) are respectively equally to the quantities \bar{t}/t and $\bar{\eta}$ in (42). Hence (B.5) and (B.6) can be used to express \bar{t} and $\bar{\eta}$ as linear functions in ε_{11} , m_0 , m_1 and m_2 (without reference to the volume fraction $\tilde{\theta}$). Performing the calculations gives

$$\begin{aligned} \bar{t} &= t \frac{(m_1 - bt\Delta)\varepsilon_{11} + \gamma(-m_0 - (1 - 3b)\Delta)}{L(m_0, m_1, m_2) + m_2 - ct^2\Delta}, \\ \bar{\eta} &= \frac{(m_2 - ct^2\Delta)\varepsilon_{11} + \gamma(-m_1 + bt\Delta)}{L(m_0, m_1, m_2) + m_2 - ct^2\Delta} \end{aligned} \quad (\text{B.7})$$

where $\Delta = (m_2m_0 - m_1^2)/g_0$. Substituting the expressions (B.7) in (B.4) gives an equation in which y is the only unknown. That equation can be written as $\varepsilon_{11} = F(y)$ where F is defined as in (53). A direct calculation gives

$$F'(y) = -\gamma \frac{L(m_0, m_1, m_2) + m_2 - ct^2\Delta}{(g_0y - bt(m_2 - ym_1) + t^2c(m_1 - ym_0))^2}$$

Let us prove that $L(m_0, m_1, m_2) + m_2 - ct^2\Delta$ is positive, i.e. that F is decreasing. It can be indeed verified from (14) that $1 - 3b > 0$ and $c - 2b(b + 3a) > 0$ whatever ν in $[0, 1/2]$. Moreover, definition (52) of the (positive) integrals m_j imply that $\Delta \leq (\eta^+)^2/g_0$. Recalling that t is assumed to be positive, we obtain

$$L(m_0, m_1, m_2) + m_2 - ct^2\Delta \geq g_0 - t^2(c + (c - 2b(b + 3a))\frac{(\eta^+)^2}{g_0})$$

Condition (48) thus ensures that

$$L(m_0, m_1, m_2) + m_2 - ct^2\Delta > 0 \quad (\text{B.8})$$

so that F is strictly decreasing on $[\eta^-, \eta^+]$. Hence the equation $\varepsilon_{11} = F(y)$ admits a (unique) solution for any ε_{11} in the interval $[F(\eta^+), F(\eta^-)]$. For $x < y$, the expression of $\tilde{\theta}(x)$ is obtained from (B.4) by replacing ε_{11} with $F(y)$ and substituting \bar{t} and $\bar{\eta}$ with the expressions in (B.7). The result is

$$\tilde{\theta}(x) = F(y) \frac{x - y}{g_0 + (1 - 3b)(m_2 - ym_1) + bt(m_1 - ym_0)} \quad (\text{B.9})$$

which corresponds to Eq. (54). Definition (52) of the integrals m_j implies that $m_2 \geq ym_1$ and $m_1 \geq ym_0$. Therefore the function $\tilde{\theta}$ in (B.9) is positive for $x > y$ and reaches its maximum at $x = \eta^+$. For later reference, we record the value taken by $\tilde{\theta}(x)$ in the limit case $\varepsilon_{11} = F(\eta^-)$. That value is denoted by $\hat{\theta}(x)$ and given by

$$\hat{\theta}(x) = F(\eta^-) \frac{x - \eta^-}{g_0 + (1 - 3b)(\langle \eta^2 \rangle - \eta^- \langle \eta \rangle) + bt(\langle \eta \rangle - \eta^-)}. \quad (\text{B.10})$$

Assume now that ε_{11} is given in $[F(\eta^+), F(\eta^-)]$ and consider the function $\tilde{\theta}$ given by (B.9) where y is such that $\varepsilon_{11} = F(y)$. It can be verified that (B.3) is satisfied for $x \leq y$. We need to check that (B.9) satisfies the constraint $0 < \tilde{\theta}(x) < 1$. Since $\tilde{\theta}$ is increasing with x , we only need to check that $\tilde{\theta}(\eta^+) \leq 1$. For $x > y$, we note from (53) and (B.9) that

$$\frac{d\tilde{\theta}(\eta^+)}{dy} = - \frac{g_0\eta^+ + bt(\eta^+m_1 - m_2) + ct^2(m_1 - \eta^+m_0)}{(g_0y - bt(m_2 - ym_1) + ct^2(m_1 - ym_0))^2}.$$

We have $m_2 \leq \eta^+m_1$ and $m_0 \leq 1$, hence

$$g_0\eta^+ + bt(\eta^+m_1 - m_2) + ct^2(m_1 - \eta^+m_0) \geq g_0\eta^+ - ct^2\eta^+.$$

Condition (48) thus ensures that $\tilde{\theta}(\eta^+)$ is decreasing with y . The condition that $\tilde{\theta}(\eta^+) \leq 1$ for all $y \in [\eta^-, \eta^+]$ is thus equivalent to $\hat{\theta}(\eta^+) \leq 1$, i.e., using (B.10),

$$\gamma(\eta^+ - \eta^-) \leq g_0\eta^- - bt(\langle \eta^2 \rangle - \eta^- \langle \eta \rangle) + ct^2(\langle \eta \rangle - \eta^-). \quad (\text{B.11})$$

Since $\eta^- \leq \langle \eta \rangle$, condition (49) ensures that (B.11) is satisfied.

Appendix B.3. Regime AM

For $\varepsilon_{11} = F(\eta^-)$, the function $\tilde{\theta}$ in (B.9) is such that $\tilde{\theta}(\eta^-) = 0$ and $\tilde{\theta}(x) \in (0, 1)$ for $x \neq \eta^-$. For a certain range of strain ε_{11} above $F(\eta^-)$, we expect a solution to (46) to be such that $\tilde{\theta}(x) \in (0, 1)$ for all x in I . The optimality condition (46) gives

$$0 = -(\varepsilon_{11} - (1 - 3b)\bar{\eta})x + \gamma - ct\bar{t} + b(t\bar{\eta} + \bar{t}x) + g_0\tilde{\theta}(x) \quad (\text{B.12})$$

for all x . Performing manipulations similar to those leading to (B.7) and recalling that $\int_{\eta^-}^{\eta^+} x^j d\tilde{p} = m_j(\eta^-) = \langle \eta^j \rangle$, we obtain

$$\begin{aligned}\bar{t} &= t \frac{(\langle \eta \rangle - btD)\varepsilon_{11} + \gamma(-1 - (1 - 3b)D)}{L(1, \langle \eta \rangle, \langle \eta^2 \rangle) + \langle \eta^2 \rangle - ct^2D}, \\ \bar{\eta} &= \frac{(\langle \eta^2 \rangle - ct^2D)\varepsilon_{11} + \gamma(-\langle \eta \rangle + btD)}{L(1, \langle \eta \rangle, \langle \eta^2 \rangle) + \langle \eta^2 \rangle - ct^2D}.\end{aligned}\tag{B.13}$$

where D is defined as in (56). Substituting (B.13) in (B.12) gives the value of $\tilde{\theta}(x)$, namely

$$\tilde{\theta}(x) = \frac{\varepsilon_{11}(x - btX_2 + ct^2X_1) - \gamma(1 + (1 - 3b)X_2 + btX_1)}{L(1, \langle \eta \rangle, \langle \eta^2 \rangle) + \langle \eta^2 \rangle - ct^2D}.\tag{B.14}$$

Expression (B.14) gives a solution to (46) as long it satisfies $0 \leq \tilde{\theta}(x) \leq 1$ for all x . Recalling that $X_i = (\langle \eta^i \rangle - x\langle \eta^{i-1} \rangle)/g_0$, we have

$$\frac{d^2\tilde{\theta}}{dx d\varepsilon_{11}} = \frac{g_0 + bt\langle \eta \rangle - ct^2}{g_0(L(1, \langle \eta \rangle, \langle \eta^2 \rangle) + \langle \eta^2 \rangle - ct^2D)}.$$

In the above expression, the denominator can be seen to be positive as a special case of (B.8) for $y = \eta^-$. The numerator is positive as a consequence of (48). It follows that $d^2\tilde{\theta}/dx d\varepsilon_{11} \geq 0$ and therefore that $d\tilde{\theta}/dx$ is increasing with ε_{11} . For $\varepsilon_{11} = F(\eta^-)$, $\tilde{\theta}$ is equal to the function $\hat{\theta}$ in (B.10) hence $d\tilde{\theta}/dx \geq d\hat{\theta}/dx$ for $\varepsilon_{11} \geq F(\eta^-)$. Since $d\hat{\theta}/dx \geq 0$, we can conclude that the function $\tilde{\theta}$ in (B.14) is increasing with x for any $\varepsilon_{11} \geq F(\eta^-)$. The condition that $\tilde{\theta}(x) \in [0, 1]$ for all x thus reduces to $\tilde{\theta}(\eta^-) \geq 0$ and $\tilde{\theta}(\eta^+) \leq 1$. Using (53) and (B.14) yields

$$\tilde{\theta}(\eta^-) = \frac{\gamma(1 + (1 - 3b)X_2 + btX_1)}{L(1, \langle \eta \rangle, \langle \eta^2 \rangle) + \langle \eta^2 \rangle - ct^2D} \left(\frac{\varepsilon_{11}}{F(\eta^-)} - 1 \right)$$

hence $\tilde{\theta}(\eta^-) \geq 0$ for $\varepsilon_{11} \geq F(\eta^-)$. Some routine calculation shows that the condition $\tilde{\theta}(\eta^+) \leq 1$ translates as $\varepsilon_{11} \leq G(\eta^+)$ where G is the function defined in (53).

Appendix B.4. Regime $M + AM$

When ε_{11} reaches $G(\eta^+)$, the function $\tilde{\theta}$ in (B.14) saturates the constraint $\tilde{\theta}(x) \leq 1$ at $x = \eta^+$. For a range of values of ε_{11} above $G(\eta^+)$, we expect the solution θ to be such

$$\tilde{\theta}(x) \in (0, 1) \text{ for } x \leq z, \tilde{\theta}(x) = 1 \text{ for } x > z\tag{B.15}$$

where $z \in I$ needs to be determined as a function of ε_{11} . For $\tilde{\theta}$ of the form (B.15), the optimality condition (46) reads as

$$\begin{aligned} 0 &= -(\varepsilon_{11} - (1 - 3b)\bar{\eta})x + \gamma - ct\bar{t} + b(t\bar{\eta} + \bar{t}x) + g_0\tilde{\theta}(x) & \text{for } x \leq z \\ 0 &\geq -(\varepsilon_{11} - (1 - 3b)\bar{\eta})x + \gamma - ct\bar{t} + b(t\bar{\eta} + \bar{t}x) + g_0 & \text{for } x > z \end{aligned} \quad (\text{B.16})$$

and the quantities \bar{t} and $\bar{\eta}$ in (42) satisfy

$$\bar{t} = t\left(\int_{\eta^-}^z \tilde{\theta}(x)d\tilde{p} + \int_z^{\eta^+} d\tilde{p}\right), \quad \bar{\eta} = \int_{\eta^-}^z x\tilde{\theta}(x)d\tilde{p} + \int_z^{\eta^+} xd\tilde{p} \quad (\text{B.17})$$

We further enforce $\tilde{\theta}$ to be continuous at z so that $\tilde{\theta}(z) = 1$. Taking the limit $x \rightarrow z$ in the second equation in (B.16) gives

$$0 = -(\varepsilon_{11} - (1 - 3b)\bar{\eta})z + \gamma + g_0 - ct\bar{t} + b(t\bar{\eta} + \bar{t}z) \quad (\text{B.18})$$

From that point, the reasoning is similar to that presented for regime $A + AM$. Multiplying the first equation in (B.16) by x^j (with $j = 0, 1$) and integrating over the interval $[\eta^-, z]$ gives the two equations

$$\begin{aligned} 0 &= -(\varepsilon_{11} - (1 - 3b)\bar{\eta})m^1 + \gamma m^0 - c\bar{t}tm^0 + b(t\bar{\eta}m^0 + \bar{t}m^1) + g_0(\bar{t}/t - 1 + m^0) \\ 0 &= -(\varepsilon_{11} - (1 - 3b)\bar{\eta})m^2 + \gamma m^1 - c\bar{t}tm^1 + b(t\bar{\eta}m^1 + \bar{t}m^2) + g_0(\bar{\eta} + m^1 - \langle \eta \rangle) \end{aligned} \quad (\text{B.19})$$

where (B.17) has been used. Solving (B.19) for $(\bar{t}, \bar{\eta})$ and substituting the result in (B.18) gives the relation $\varepsilon_{11} = G(z)$ where G is defined as in (53). For $x \geq z$, it follows that $\tilde{\theta}(x)$ is given by

$$\tilde{\theta}(x) = 1 + \frac{(\gamma + g_0 + bt\langle \eta \rangle - t^2c)(x - z)}{g_0z - bt(m^2 - zm^1) + t^2c(m^1 - zm^0)} \quad (\text{B.20})$$

which corresponds to Eq. (57). The function G can be verified to be decreasing on $[\eta^-, \eta^+]$ so that the equation $\varepsilon_{11} = G(z)$ admits a unique solution for ε_{11} in the interval $[G(\eta^+), G(\eta^-)]$. Under condition (49), the function $\tilde{\theta}$ in (B.20) is found to satisfy the constraint $0 \leq \tilde{\theta}(x) \leq 1$ for all (x, z) in I^2 and any given ε_{11} in $[G(\eta^-), G(\eta^+)]$ (details of that verification are omitted here for the sake of brevity).

Appendix B.5. Regime M

For $\varepsilon_{11} \geq G(\eta^-)$, we show that $\tilde{\theta} = 1$ a solution to (46). Note from (47) that $\bar{t} = t$ and $\bar{\eta} = \langle \eta \rangle$ when $\tilde{\theta} = 1$. We thus obtain from (46) that $\tilde{\theta} = 1$ is a solution if

$$0 \geq -(\varepsilon_{11} - (1 - 3b)\langle \eta \rangle)x + \gamma - ct^2 + bt(\langle \eta \rangle + x) + g_0 \text{ for all } x. \quad (\text{B.21})$$

It can easily be verified from (53) that $G(\eta^-) \geq (1 - 3b)\langle\eta\rangle + bt$. The right hand side of (B.21) is thus decreasing with x , so that (B.21) is equivalent to

$$0 \geq -(\varepsilon_{11} - (1 - 3b)\langle\eta\rangle)\eta^- + \gamma - ct^2 + bt(\langle\eta\rangle + \eta^-) + g_0. \quad (\text{B.22})$$

Using (53), the right-hand of (B.22) is found to vanish for $\varepsilon_{11} = G(\eta^-)$. It follows that $\bar{\theta} = 1$ is a solution to (46) for any $\varepsilon_{11} \geq G(\eta^-)$.

Appendix C. Convexity of Φ

In this section we study the convexity of the quadratic functional Φ in (28), i.e. we study if

$$\bar{\tau}_{11}(\theta)^2 + g_0 \int_{\text{SO}(3)} p(\mathbf{r})\theta^2(\mathbf{r})d\mu - 2a(\text{tr } \bar{\tau}(\theta))^2 - 2b\|\bar{\tau}(\theta)\|^2 \geq 0 \quad (\text{C.1})$$

for all θ . Note that (C.1) can be rewritten as

$$\langle\theta, T\theta\rangle_p \geq 0 \quad (\text{C.2})$$

where $T\theta$ is the function defined on $\text{SO}(3)$ by

$$(T\theta)(\mathbf{r}) = g_0\theta(\mathbf{r}) + \int_{\mathbf{s} \in \text{SO}(3)} (\eta(\mathbf{r})\eta(\mathbf{s}) - 2at^2 - 2b\boldsymbol{\eta}(\mathbf{r}) : \boldsymbol{\eta}(\mathbf{s}))\theta(\mathbf{s})p(\mathbf{s})d\mu \quad (\text{C.3})$$

and $\langle\Theta, \Theta'\rangle_p = \int_{\text{SO}(3)} \Theta(\mathbf{r})\Theta'(\mathbf{r})p(\mathbf{r})d\mu$. In the following, we use the fact that the operator T is diagonalizable and study its eigenvalues. Since T acts on a space of infinite dimension, the concept of diagonalization calls for some mathematical justification. Let $L^2(\text{SO}(3), p d\mu)$ be the space of square-integrable functions on $\text{SO}(3)$ for the measure $p d\mu$, i.e. the space of functions $\theta : \text{SO}(3) \mapsto \mathbb{R}$ verifying $\langle\theta, \theta\rangle_p < +\infty$. The space $L^2(\text{SO}(3), p d\mu)$ is a Hilbert space for the scalar product $\langle\cdot, \cdot\rangle_p$. Observe that the operator T in (C.3) is self-adjoint, i.e. verifies $\langle\theta', T\theta\rangle_p = \langle\theta, T\theta'\rangle_p$ for any θ and θ' in $L^2(\text{SO}(3), p d\mu)$. Moreover, the integral operator $T - g_0I$ is of the Hilbert-Schmidt type – and therefore compact – because its kernel $(\mathbf{r}, \mathbf{s}) \mapsto \eta(\mathbf{r})\eta(\mathbf{s}) - 2at^2 - 2b\boldsymbol{\eta}(\mathbf{r}) : \boldsymbol{\eta}(\mathbf{s})$ is bounded (Reed and Simon, 1980). The Hilbert-Schmidt theorem for self-adjoint compact operators implies the existence of a complete orthonormal basis $\{\theta_n\}$ of $L^2(\text{SO}(3), p d\mu)$ such that $T\theta_n - g_0\theta_n = \mu_n\theta_n$ with $\mu_n \rightarrow 0$ as $n \rightarrow \infty$. Setting $\lambda_n = \mu_n + g_0$, we obtain that $T\theta_n = \lambda_n\theta_n$ and

$$\langle\theta, T\theta\rangle_p = \sum_{n=0}^{\infty} \lambda_n \langle\theta, \theta_n\rangle_p^2$$

for any $\theta \in L^2(\text{SO}(3), p d\mu)$. Proving that the eigenvalues of T are positive ensures that $\langle \theta, T\theta \rangle_p \geq 0$. We are thus led to consider the eigenvalue problem

$$g_0\theta(\mathbf{r}) + \bar{\tau}_{11}(\theta)\eta(\mathbf{r}) - 2at(\text{tr } \bar{\tau}(\theta)) - 2b\bar{\tau}(\theta) : \boldsymbol{\eta}(\mathbf{r}) = \lambda\theta(\mathbf{r}) \quad (\text{C.4})$$

with $\bar{\tau}(\theta)$ defined as in (26). In the following we consider the general situation where $t \neq 0$ but the reasoning can easily be adapted to the case $t = 0$. Integrating (C.4) over $\text{SO}(3)$ yields

$$g_0 \frac{\text{tr } \bar{\tau}(\theta)}{t} + \bar{\tau}_{11}(\theta)\langle \eta \rangle - 2at(\text{tr } \bar{\tau}(\theta)) - 2b\bar{\tau}(\theta) : \mathbf{X} = \lambda \frac{\text{tr } \bar{\tau}(\theta)}{t} \quad (\text{C.5})$$

with $\mathbf{X} = \int_{\text{SO}(3)} \boldsymbol{\eta}(\mathbf{r})p(\mathbf{r})d\mu$ and the relation $\text{tr } \bar{\tau}(\theta) = t \int_{\text{SO}(3)} \theta(\mathbf{r})p(\mathbf{r})d\mu$ has been used. Note that $X_{11} = \langle \eta \rangle$ and $\text{tr } \mathbf{X} = t$. Since the function i is transversely isotropic, Property 1 implies that

$$\mathbf{X} = \langle \eta \rangle \mathbf{u}_1 \otimes \mathbf{u}_1 + \frac{1}{2}(t - \langle \eta \rangle)(\mathbf{u}_2 \otimes \mathbf{u}_2 + \mathbf{u}_3 \otimes \mathbf{u}_3).$$

Replacing in (C.5) leads to

$$g_0 \frac{\text{tr } \bar{\tau}(\theta)}{t} + (1 - 3b)\bar{\tau}_{11}(\theta)\langle \eta \rangle - ct \text{tr } \bar{\tau}(\theta) + b(t\bar{\tau}_{11}(\theta) + \langle \eta \rangle \text{tr } \bar{\tau}(\theta)) = \lambda \frac{\text{tr } \bar{\tau}(\theta)}{t}. \quad (\text{C.6})$$

An other relation between $\text{tr } \bar{\tau}(\theta)$ and $\bar{\tau}_{11}(\theta)$ is obtained by multiplying (C.4) by $\eta(\mathbf{r})$ and integrating over $\text{SO}(3)$. Omitting the detail of the calculations, we obtain

$$g_0\bar{\tau}_{11}(\theta) + (1 - 3b)\bar{\tau}_{11}(\theta)\langle \eta^2 \rangle - ct\langle \eta \rangle \text{tr } \bar{\tau}(\theta) + b(t\langle \eta \rangle \bar{\tau}_{11}(\theta) + \langle \eta^2 \rangle \text{tr } \bar{\tau}(\theta)) = \lambda \bar{\tau}_{11}(\theta) \quad (\text{C.7})$$

Consider an eigenvalue λ distinct from the (positive) value $g_0 + bt\langle \eta \rangle + (1 - 3b)\langle \eta^2 \rangle$. Then we obtain from (C.7) that

$$\bar{\tau}_{11}(\theta) = \frac{c\langle \eta \rangle t - b\langle \eta^2 \rangle}{g_0 + bt\langle \eta \rangle + (1 - 3b)\langle \eta^2 \rangle - \lambda} \text{tr } \bar{\tau}(\theta). \quad (\text{C.8})$$

Substituting in (C.6) gives

$$0 = (\lambda^2 - B\lambda + C)\text{tr } \bar{\tau}(\theta) \quad (\text{C.9})$$

with $B = 2g_0 + (1 - 3b)\langle \eta^2 \rangle + 2bt\langle \eta \rangle - ct^2$ and $C = g_0(L(1, \langle \eta \rangle, \langle \eta^2 \rangle) + \langle \eta^2 \rangle - ct^2D)$. Two cases need to be discussed. If $\text{tr } \bar{\tau}(\theta) \neq 0$, then necessarily $\lambda^2 - B\lambda + C = 0$. Condition (48) implies that $g_0 \geq ct^2$ and therefore that $B \geq 0$. Condition (48) also

ensures that $C \geq 0$ as a special case of (B.8) for $y = \eta^-$. It follows that the solutions to the equation $0 = \lambda^2 - B\lambda + C$ (if any) are positive. Let us now consider the case $\text{tr } \bar{\boldsymbol{\tau}}(\theta) = 0$. In that case, we note from (C.8) that $\bar{\tau}_{11}(\theta) = 0$. Eq. (C.4) becomes

$$g_0\boldsymbol{\theta}(\mathbf{r}) - 2b\bar{\boldsymbol{\tau}}(\theta) : \boldsymbol{\eta}(\mathbf{r}) = \lambda\boldsymbol{\theta}(\mathbf{r}).$$

Multiplying that equation by $\boldsymbol{\eta}(\mathbf{r})$ and integrating over $\text{SO}(3)$ yields

$$\frac{g_0 - \lambda}{2b} \bar{\boldsymbol{\tau}}(\theta) = \mathbb{Q} : \bar{\boldsymbol{\tau}}(\theta) \quad (\text{C.10})$$

where

$$\mathbb{Q} = \int_{\text{SO}(3)} \boldsymbol{\eta}(\mathbf{r}) \otimes \boldsymbol{\eta}(\mathbf{r}) p(\mathbf{r}) d\mu.$$

Relation (C.10) shows that $(g_0 - \lambda)/2b$ is an eigenvalue of the fourth-order tensor \mathbb{Q} . Note that \mathbb{Q} is positive and symmetric. Moreover, since p and i are transversely isotropic, the tensor \mathbb{Q} is also transversely isotropic. It follows that \mathbb{Q} has the matrix representation (using Mandel notation)

$$\mathbb{Q} = \begin{pmatrix} \langle \eta^2 \rangle & \langle \eta\eta_{22} \rangle & \langle \eta\eta_{22} \rangle & 0 & 0 & 0 \\ \langle \eta\eta_{22} \rangle & \langle \eta_{22}^2 \rangle & \langle \eta_{22}\eta_{33} \rangle & 0 & 0 & 0 \\ \langle \eta\eta_{22} \rangle & \langle \eta_{22}\eta_{33} \rangle & \langle \eta_{22}^2 \rangle & 0 & 0 & 0 \\ 0 & 0 & 0 & 2\langle \eta_{23}^2 \rangle & 0 & 0 \\ 0 & 0 & 0 & 0 & 2\langle \eta_{12}^2 \rangle & 0 \\ 0 & 0 & 0 & 0 & 0 & 2\langle \eta_{12}^2 \rangle \end{pmatrix} \quad (\text{C.11})$$

where, e.g.,

$$\langle \eta_{12}^2 \rangle = \int_{\text{SO}(3)} \eta_{12}^2(\mathbf{r}) p(\mathbf{r}) d\mu. \quad (\text{C.12})$$

The eigenvalues and eigenvectors of \mathbb{Q} can be obtained in closed-form in terms of $\langle \eta_{12}^2 \rangle$ and other average quantities that appear in (C.11). Since the tensor $\bar{\boldsymbol{\tau}}(\theta)$ in (C.10) satisfies $\bar{\tau}_{11}(\theta) = \text{tr } \bar{\boldsymbol{\tau}}(\theta) = 0$, only the eigenspaces containing tensors $\bar{\boldsymbol{\tau}}$ such that $\bar{\tau}_{11} = \text{tr } \bar{\boldsymbol{\tau}} = 0$ are of concern. The corresponding eigenvalues of \mathbb{L} are $2\langle \eta_{12}^2 \rangle$, $2\langle \eta_{23}^2 \rangle$ and $\langle \eta_{22}^2 \rangle - \langle \eta_{22}\eta_{33} \rangle$. Checking that $\lambda \geq 0$ is thus a matter of checking that $g_0 - 2b\mu \geq 0$ for $\mu \in \{2\langle \eta_{12}^2 \rangle, 2\langle \eta_{23}^2 \rangle, \langle \eta_{22}^2 \rangle - \langle \eta_{22}\eta_{33} \rangle\}$. For a given texture, those quantities can be easily be calculated numerically. Conditions that are independent of the texture can be obtain by looking for the maximum values taken $\langle \eta_{12}^2 \rangle$, $\langle \eta_{23}^2 \rangle$ and $\langle \eta_{22}^2 \rangle - \langle \eta_{22}\eta_{33} \rangle$ over transversely isotropic textures. To that purpose, it is convenient

to parameterize rotations by their axis \mathbf{n} and their angle $\omega \in [0, \pi]$. We further parameterize the unit vector \mathbf{n} using angles $(\phi_1, \phi_2) \in [0, \pi] \times [0, 2\pi]$ such that

$$\mathbf{n} = \cos \phi_1 \mathbf{u}_1 + \sin \phi_1 (\cos \phi_2 \mathbf{u}_2 + \sin \phi_2 \mathbf{u}_3).$$

Using that parameterization, the ODF p and the tensor $\boldsymbol{\eta}$ can be viewed as functions of (ω, ϕ_1, ϕ_2) . The assumption that p is transversely isotropic means that p is actually independent of ϕ_2 . In terms of (ω, ϕ_1, ϕ_2) , the expression of the Haar measure is $d\mu = (\sin^2 \frac{1}{2}\omega \sin \phi_1) / 2\pi^2 d\omega d\phi_1 d\phi_2$ (Miles, 1965). Hence

$$\langle \eta_{12}^2 \rangle = \frac{1}{2\pi^2} \int_{(\omega, \phi_1)} M_{12}(\omega, \phi_1) p(\omega, \phi_1) \sin^2 \frac{\omega}{2} \sin \phi_1 d\omega d\phi_1$$

where

$$M_{12}(\omega, \phi_1) = \int_0^{2\pi} \eta_{12}^2(\omega, \phi_1, \phi_2) d\phi_2.$$

Since p is positive and satisfies $\int_{\text{SO}(3)} p(\mathbf{r}) d\mu = 1$, we have

$$\langle \eta_{12}^2 \rangle \leq \sup_{\omega, \phi_1} M_{12}(\omega, \phi_1).$$

For given values of the lattice parameters, $\sup M_{12}$ can be estimated numerically. If $g_0 - 4b \sup M_{12} > 0$, then $g_0 - 4b \langle \eta_{12}^2 \rangle > 0$ for any transversely isotropic texture. This procedure is easily adapted to bound $\langle \eta_{23}^2 \rangle$ and $\langle \eta_{22}^2 \rangle - \langle \eta_{22}\eta_{33} \rangle$ independently of the texture. Calculating those bounds numerically for the lattice parameters in Table 1 shows that $g_0 - 2b\mu \geq 0$ for $\mu \in \{2\langle \eta_{12}^2 \rangle, 2\langle \eta_{23}^2 \rangle, \langle \eta_{22}^2 \rangle - \langle \eta_{22}\eta_{33} \rangle\}$, independently of the texture. This completes the verification that any eigenvalue λ of T is positive, and therefore that the functional Φ is convex.

References

- Alessi, R., Pham, K., 2016. Variational formulation and stability analysis of a three dimensional superelastic model for shape memory alloys. *Journal of the Mechanics and Physics of Solids* 87, 150–176.
- Bechle, N. J., Kyriakides, S., 2014. Localization in NiTi tubes under bending. *International Journal of Solids and Structures* 51 (5), 967–980.
- Bechle, N. J., Kyriakides, S., 2016. Evolution of localization in pseudoelastic NiTi tubes under biaxial stress states. *International Journal of Plasticity* 82, 1–31.

- Besson, J., Cailletaud, G., Chaboche, J.-L., Forest, S., 2009. Non-linear mechanics of materials. Vol. 167. Springer.
- Bhattacharya, K., 2003. Microstructure of martensite: why it forms and how it gives rise to the shape-memory effect. Oxford University Press.
- Bogachev, V. I., 2007. Measure theory. Springer.
- Brinson, L. C., Schmidt, I., Lammering, R., 2004. Stress-induced transformation behavior of a polycrystalline NiTi shape memory alloy: micro and macromechanical investigations via in situ optical microscopy. *Journal of the Mechanics and Physics of Solids* 52 (7), 1549–1571.
- Bunge, H.-J., 2013. Texture analysis in materials science: mathematical methods. Elsevier.
- Butler, J., 1962. Lüders front propagation in low carbon steels. *Journal of the Mechanics and Physics of Solids* 10 (4), 313–318.
- Churchill, C., Shaw, J., Iadicola, M., 2009. Tips and tricks for characterizing shape memory alloy wire: Part 3-localization and propagation phenomena. *Experimental Techniques* 33, 70–78.
- Considère, A., 1885. *Annales des Ponts et Chaussees* 9, 574–775.
- Daly, S., Ravichandran, G., Bhattacharya, K., 2007. Stress-induced martensitic phase transformation in thin sheets of Nitinol. *Acta Materialia* 55 (10), 3593–3600.
- Drucker, D. C., 1959. A definition of stable inelastic material. *Journal of Applied Mechanics* 26, 101–195.
- Ericksen, J. L., 1975. Equilibrium of bars. *Journal of Elasticity* 5 (3), 191–201.
- Govindjee, S., Hackl, K., Heinen, R., 2007. An upper bound to the free energy of mixing by twin-compatible lamination for n -variant martensitic phase transformations. *Continuum Mechanics and Thermodynamics* 18 (7), 443–453.
- Govindjee, S., Mielke, A., Hall, G., 2003. The free energy of mixing for n -variant martensitic phase transformations using quasi-convex analysis. *J. Mech. Phys. Solids* 51 (4).
- Hackl, K., Heinen, R., 2008. An upper bound to the free energy of n -variant polycrystalline shape memory alloys. *J.Mech.Phys.Solids* 56, 2832–2843.

- Hackl, K., Heinen, R., Schmahl, W. W., Hasan, M., 2008. Experimental verification of a micromechanical model for polycrystalline shape memory alloys in dependence of martensite orientation distributions. *Materials Science and Engineering: A* 481, 347–350.
- Hallai, J. F., Kyriakides, S., 2013. Underlying material response for Lüders-like instabilities. *International Journal of Plasticity* 47, 1–12.
- Hannequart, P., Peigney, M., Caron, J.-F., 2019. A micromechanics-based model for polycrystalline Ni–Ti wires. *Smart Materials and Structures* 28 (8), 085040.
- Hill, R., 1958. A general theory of uniqueness and stability in elastic-plastic solids. *Journal of the Mechanics and Physics of Solids* 6 (3), 236–249.
- Iadicola, M. A., Shaw, J. A., 2004. Rate and thermal sensitivities of unstable transformation behavior in a shape memory alloy. *International Journal of Plasticity* 20 (4-5), 577–605.
- Knowles, K., Smith, D., 1981. The crystallography of the martensitic transformation in equiatomic nickel-titanium. *Acta Metallurgica* 29 (1), 101–110.
- Kohn, R. V., 1991. The relaxation of a double-well energy. *Continuum Mechanics and Thermodynamics* 3 (3), 193–236.
- Kyriakides, S., Miller, J., 2000. On the propagation of Lüders bands in steel strips. *J. Appl. Mech.* 67 (4), 645–654.
- Liu, Y., Xie, Z. L., Van Humbeeck, J., Delaey, L., 1999. Effect of texture orientation on the martensite deformation of NiTi shape memory alloy sheet. *Acta materialia* 47 (2), 645–660.
- Lüders, W., 1860. Über die äusserung der elasticität an stahlartigen eisenstäben und stahlstäben, und über eine beim biegen solcher stäbe beobachtete molecularbewegung. *Dingler’s Polytechnic Journal* 155, 18–22.
- Miles, R. E., 1965. On random rotations in R^3 . *Biometrika* 52 (3/4), 636–639.
- Nae, F. A., Matsuzaki, Y., Ikeda, T., 2002. Micromechanical modeling of polycrystalline shape-memory alloys including thermo-mechanical coupling. *Smart Materials and Structures* 12 (1), 6.
- Otsuka, K., Nakamura, T., Shimizu, K., 1974. Electron microscopic study of b1-martensite in Cu–Al–Ni single crystal. *Trans. Jap. Inst. Met* 15, 200.

- Otsuka, K., Sawamura, T., Shimizu, K., 1971. Crystal structure and internal defects of equiatomic TiNi martensite. *Physica status solidi (a)* 5 (2), 457–470.
- Otsuka, K., Shimizu, K., 1974. Morphology and crystallography of thermoelastic Cu–Al–Ni martensite analyzed by the phenomenological theory. *Transactions of the Japan Institute of Metals* 15 (2), 103–108.
- Peigney, M., 2008. Recoverable strains in composite shape memory alloys. *J. Mech. Phys. Solids* 56 (2), 360–375.
- Peigney, M., 2009. A non-convex lower bound on the effective free energy of polycrystalline shape memory alloys. *J.Mech.Phys.Solids* 57, 970–986.
- Peigney, M., 2013a. On the energy-minimizing strains in martensitic microstructures-part 1: Geometrically nonlinear theory. *J.Mech.Phys.Solids* 61, 1489–1510.
- Peigney, M., 2013b. On the energy-minimizing strains in martensitic microstructures-part 2: Geometrically linear theory. *J.Mech.Phys.Solids* 61, 1511–1530.
- Peigney, M., 2023. A micromechanically consistent energy estimate for polycrystalline shape-memory alloys. I - general formulation. *Journal of the Mechanics and Physics of Solids* 172, 105165.
- Piobert, G., 1842. *Expérience sur la pénétration des projectiles dans le fer forgé*. Vol. 595.
- Reed, M., Simon, B., 1980. *Methods of Modern Mathematical Physics: Functional Analysis*; Rev. ed. Academic press.
- Reedlunn, B., Churchill, C. B., Nelson, E. E., Shaw, J. A., Daly, S. H., 2014. Tension, compression, and bending of superelastic shape memory alloy tubes. *Journal of the Mechanics and Physics of Solids* 63, 506–537.
- Reedlunn, B., LePage, W. S., Daly, S. H., Shaw, J. A., 2020. Axial-torsion behavior of superelastic tubes: Part I, proportional isothermal experiments. *International Journal of Solids and Structures* 199, 1–35.
- Shaw, J. A., 2000. Simulations of localized thermo-mechanical behavior in a NiTi shape memory alloy. *International journal of plasticity* 16 (5), 541–562.
- Shaw, J. A., Kyriakides, S., 1997. On the nucleation and propagation of phase transformation fronts in a NiTi alloy. *Acta materialia* 45 (2), 683–700.

- Shield, T., 1995. Orientation dependence of the pseudoelastic behavior of single crystals of CuAlNi in tension. *Journal of the Mechanics and Physics of Solids* 43 (6), 869–895.
- Shu, Y., Bhattacharya, K., 1998. The influence of texture on the shape-memory effect in polycrystals. *Acta Materialia* 46 (15), 5457–5473.
- Sittner, P., Liu, Y., Novák, V., 2005. On the origin of Lüders-like deformation of NiTi shape memory alloys. *Journal of the Mechanics and Physics of Solids* 53 (8), 1719–1746.
- Smyshlyaev, V., Willis, J., 1998. A non-local variational approach to the elastic energy minimalization of martensitic polycrystals. *Proceedings of the Royal Society of London. Series A: Mathematical, Physical and Engineering Sciences* 454 (1974), 1573–1613.
- Sun, Q.-P., Li, Z.-Q., 2002. Phase transformation in superelastic NiTi polycrystalline micro-tubes under tension and torsion—from localization to homogeneous deformation. *International Journal of Solids and Structures* 39 (13-14), 3797–3809.
- Willis, J. R., 1977. Bounds and self-consistent estimates for the overall properties of anisotropic composites. *Journal of the Mechanics and Physics of Solids* 25 (3), 185–202.
- Ye, Y., 2011. Interior point algorithms: theory and analysis. Vol. 44. John Wiley & Sons.